https://doi.org/10.5194/egusphere-2025-2667
Preprint. Discussion started: 7 July 2025

Impacts of summertime photochemical aging on the physicochemical properties of aerosols in a Paris suburban forest region

Chenjie Yu[1], Paola Formenti[1], Joel F. de Brito[2], Astrid Bauville[3], Antonin Bergé[3], Hichem Bouzidi[1], Mathieu Cazaunau[1], Manuela Cirtog[3], Claudia Di Biagio[1], Ludovico Di Antonio[3*], Cécile Gaimoz[3], Franck Maisonneuve[3], Pascal Zapf[1], Tobias Seubert[4], Simone T. Andersen[4], Patrick Dewald[4], Gunther N. T. E. Türk[4], John N. Crowley[4], Alexandre Kukui[5], Chaoyang Xue[5,6], Cyrielle Denjean[7], Olivier Garrouste[7], Jean-Claude Etienne[7], Huihui Wu[8,3], James D. Allan[8,9], Dantong Liu[10], Yangzhou Wu[11], Christopher Cantrell[3], and Vincent Michoud[1]

[1] Université Paris Cité and Univ Paris Est Créteil, CNRS, LISA, F-75013 Paris, France
[2] IMT Nord Europe, Institut Mines-Télécom, Université de Lille, Centre for Energy and Environment, F-59000, Lille, France
[3] Univ Paris Est Créteil and Université Paris Cité, CNRS, LISA, F-94010 Créteil, France
[4] Atmospheric Chemistry Department, Max-Planck-Institute for Chemistry, 55128-Mainz, Germany
[5] Laboratoire de Physique et Chimie de l'Environnement et de l'Espace (LPC2E), CNRS−Université Orléans−CNES, Orléans Cedex 245071, France
[6] Multiphase Chemistry Department, Max-Planck-Institute for Chemistry, 55128-Mainz, Germany
[7] CNRM, Universite de Toulouse, Meteo-France, CNRS, Toulouse, France
[8] Department of Earth and Environmental Sciences, University of Manchester, Manchester M13 9PL, United Kingdom
[9] National Centre for Atmospheric Sciences, University of Manchester, Manchester M13 9PL, United Kingdom
[10] Department of Atmospheric Sciences, School of Earth Sciences, Zhejiang University, Zhejiang 310027, China
[11] Guangxi Key Laboratory of Theory and Technology for Environmental Pollution Control, Collaborative Innovation Center for Water Pollution Control and Water Safety in Karst Area, Guilin University of Technology, Guilin, China
[*] Now at : Laboratoire, Atmosphères, Observations Spatiales (LATMOS)/IPSL, Sorbonne Université, UVSQ, CNRS, 75252 Paris, France

Correspondence to: Chenjie Yu (chenjie.yu@lisa.ipsl.fr) and Paola Formenti (paola.formenti@lisa.ipsl.fr)

Abstract.

Organic Aerosols (OA), which significantly affect the climate system and human health, often contain a substantial fraction of atmospherically processed species known collectively as Oxygenated Organic Aerosol (OOA). However, the formation pathways and evolution of OOA remain poorly understood. To address this need, an experiment was conducted in a suburban forest in the Paris region to systematically study the evolution of OOA and their optical properties. Our results show that the photochemical processes drove significant increases in total submicron particle mass concentrations in the forest site, primarily via the production of OOA derived from both biogenic and anthropogenic emissions. Air mass origin critically influenced Particulate Matter (PM) pollution levels and photochemical activity: under elevated pollution and intense solar radiation during continental air mass-dominated periods, rapid formation of More-Oxidized OOA (MO-OOA) occurred. This MO-OOA dominated Brown Carbon (BrC) contributions, enhancing short-wavelength light absorption by 35% on average after a relative ~24-hour photochemical aging process. Conversely, periods dominated by clean maritime air masses featured humid, low-radiation conditions that yielded reduced pollution levels and an increased proportion of nitrogen-enriched, Less-Oxidized OOA (LO-OOA). Suppressed photochemical activity during the clean maritime period

https://doi.org/10.5194/egusphere-2025-2667
Preprint. Discussion started: 7 July 2025

limited MO-OOA production, resulting in a lower overall oxidation state of OA. These findings underscore the dual role of photochemistry in shaping aerosol optical properties and climate impacts, highlighting the necessity of accounting for air mass dynamics and oxidation pathways in suburban forest regions.

1. Introduction

Atmospheric aerosols are complex combinations of different chemical species and have an important impact on the climate system by scattering and absorbing atmospheric radiation (Ravishankara et al., 2015) and by interacting with clouds (Farmer et al., 2015). They also negatively affect air quality by reducing visibility, causing respiratory problems, and damaging ecosystems (Manisalidis et al., 2020). Rapid urbanization and industrial activities have led to high levels of anthropogenic aerosol emissions in developed megacities (Shi et al., 2019). Therefore, characterizing the physicochemical properties of aerosols is crucial for understanding their impact on climate, air quality, and human health, ultimately informing strategies for mitigation and environmental protection.

Aerosols contain various components varying from volatile to refractory materials. Globally, Organic Aerosols (OA) often comprise the dominated mass fraction of submicron aerosols, while other components include soot (also known as Black Carbon (BC)), inorganic salts (such as sulfates, nitrates, and ammonium), metals, and other elements (Seinfeld and Pandis, 2016). OA can be classified into primary OA (POA) and secondary OA (SOA) compounds. POA compounds are hydrocarbon components emitted from primary sources such as biomass burning, cooking, and transport (e.g. (Allan et al., 2010; Lu et al., 2011)), while SOA compounds are formed through atmospheric chemical reactions involving the oxidation of gas precursors such as volatile organic compounds (VOCs) (Kroll and Seinfeld, 2008). Source apportionment analysis on OA based on mass spectra from widely used instruments such as the Aerosol Mass Spectrometer (AMS) (Jayne et al., 2000) or Aerosol Chemical Speciation Monitor (ACSM) (Ng et al., 2011) can provide insight into its primary and secondary components. The derived POA typically includes hydrocarbon-like OA (HOA), biomass burning OA (BBOA), and cooking-related OA (COA), while the SOA (also referred as oxygenated OA (OOA), often used as a proxy for SOA) is often typically separated into Less-Oxidized OOA (LO-OOA) and More-Oxidized OOA (MO-OOA). At some measurement sites, specific components like peat-emitted OA, shipping-related OA, or sea spray-related OA can also be identified (Lin et al., 2020; Fossum et al., 2024; Schmale et al., 2013). Previous AMS/ACSM studies revealed that the OOA dominated the total submicron OA mass in the European region with a yearly average fraction of more than 70%, while the contribution from solid-fuel related POA is about 16% yearly on average and mostly during the winter months (Chen et al., 2022). The chemical characteristics and evolution of OA have significant impacts on aerosol optical properties. Particulate Organic Nitrate (pON), an important part of OA formed either through primary emissions or through the oxidation of VOCs in the presence of nitrogen oxide radicals and atmospheric oxidants, can significantly contribute to total light-absorbing Brown Carbon (BrC) loadings (Laskin et al., 2015). Studies show that the contribution of light absorption by BrC may be enhanced

https://doi.org/10.5194/egusphere-2025-2667
Preprint. Discussion started: 7 July 2025

due to the increase of nitrogenous organic aerosols during photochemical aging (Yang et al., 2021; Jiang et al., 2022; Cappa et al., 2020). However, bleaching of BrC through intensive photooxidation processes has also been documented, with reported timescales exhibiting significant variability depending on factors such as oxidant concentrations and ambient relative humidity (RH) (Liu et al., 2021; Zhao et al., 2015). In addition to its impacts on aerosol optical properties, the variability of OOA also influences the aerosol hygroscopicity. It is known that the complex aging process of OOA introduces significant uncertainty in understanding the cloud condensation nuclei (CCN) activity of atmospheric aerosols (Mei et al., 2013; Wang et al., 2022). Given all these factors, understanding the aging process of OA is crucial to better constrain their role in the atmosphere.

Paris is one of the most developed and densely populated megacities in Europe, facing significant air pollution challenges. In the past decades, extensive research has been conducted to identify and characterize the properties of particulate pollutants in the Paris region (e.g. (Beekmann et al., 2015)). Previous aerosol mass spectrometer studies (Stirnberg et al., 2021; Bressi et al., 2013; Petit et al., 2015; Healy et al., 2013) indicate that Paris is often affected by the mid-range to long-range transport pollutants attribute to the flat orography of the city. Previous AMS Positive Matrix Factorization (PMF) analysis during summertime have shown that, in addition to the significant contributions from the continental polluted airmass to the total PM_1, Paris is also influenced by emissions from the Atlantic Ocean (Crippa et al., 2013). Zhang et al. (2019) observed a significant increase in LO-OOA related to the mixture of anthropogenic and biogenic emissions in Paris during the summer, but the formation mechanism remains poorly understood. This knowledge gap is potentially because previous studies in the Paris region mostly concentrated on developed areas. As Paris is surrounded by forest regions, it is important to address the issue of how the mixture of anthropogenic and biogenic emissions impacts secondary aerosol properties in this region. Furthermore, it is reported that the Ozone (O_3) has become an important pollutant in the urban areas, and the decreasing of Nitrogen Oxides (NO_x) may contribute to the increases in European urban O_3 concentrations in the future (Grange et al., 2021). Measurements in a suburban forest region in China indicate that the oxidation of Biogenic VOCs (BVOCs) by O_3 may lead to enhanced formation of LO-OOA (Gao et al., 2023). Therefore, characterizing the evolution of aerosol physicochemical properties during transport is crucial, given the changing atmospheric oxidation capacity. To address these issues, the Atmospheric Chemistry of the Suburban Forest (ACROSS) project was designed to investigate aerosol physicochemical properties in a suburban forest area of Paris (Cantrell and Michoud, 2022). In this study, the evolution of aerosol composition was systematically examined as a function of photochemical processes, with a focused analysis of their subsequent effects on aerosol physicochemical properties under ambient conditions.

https://doi.org/10.5194/egusphere-2025-2667
Preprint. Discussion started: 7 July 2025

2. Experimental methods and data analysis

2.1 Atmospheric Chemistry of the Suburban Forest (ACROSS) project

A ground-based experiment was conducted in a suburban forest area of Paris (Rambouillet forest) within the framework of the ACROSS project (Cantrell and Michoud, 2022). The broader ACROSS Rambouillet experiment, encompassing both near-ground (~5 m) and above-canopy (on a ~40-m-high tower) measurements, was conducted from June 13th to July 25th, 2022. In this study, the scope is confined to near-ground measurements to facilitate a focused discussion on regional pollution within the boundary layer. The analysis period is refined to June 29th to July 20th, ensuring instrument availability.

2.2 Particulate phase measurements

2.2.1 High-Resolution Time-of-Flight Aerosol Mass Spectrometer (HR-AMS)

The Non-Refractory Particulate Matter with aerodynamic diameter less than 1 μm (NR-PM_1) compositions, including organic (OA), sulfate (SO_4), nitrate (NO_3), ammonium (NH_4), and chloride (Chl), was characterised through an Aerodyne HR-AMS (Decarlo et al., 2006). Briefly, particles enter the AMS through a critical orifice and an aerodynamic lens, forming a narrow particle beam. The particle size (vacuum aerodynamic diameter) is determined in a Particle Time-of-Flight (PToF) region through the flight time of particles. NR components are subsequently vaporized on a metallic surface, ionized by electron impact ionization (EI, 70 eV), and analysed by Time-of-Flight Mass Spectrometry (ToF-MS) under high vacuum. During the campaign, the HR-AMS conducted the measurements with a flow rate of ~0.1 L min^{-1} from a $PM_{2.5}$ (particulate matter with aerodynamic diameter less than 2.5 μm) cyclone and through a Nafion dryer. The HR-AMS sampled intermittently, alternating between near-ground and above-canopy measurements every 5 minutes. This study focuses exclusively on data collected at near-ground level. The HR-AMS was operated alternatively among two modes: V-mode and PToF mode. The Ionization Efficiency (IE) and the Relative Ionization Efficiency (RIE) of the HR-AMS were calibrated using mono-disperse (300 nm), nebulized ammonium nitrate and ammonium sulfate particles, and a Composition-Dependent Collection Efficiency (CDCE) was applied to the final results.

The mass concentrations of different NR-PM_1 species and high-resolution mass spectra analysis were processed from the V-mode results. Elemental ratios of OA, including oxygen-to-carbon (O:C), hydrogen-to-carbon (H:C), and nitrogen-to-carbon (N:C), as well as the organic mass to organic carbon (OM:OC), were derived from high-resolution mass spectra using the "Improved-Ambient (I-A)" method (Canagaratna et al., 2015). The contribution of particle-phase organic nitrate (pON) to the total HR-AMS measured NO3 is estimated following the method described by Day et al. (2022), as shown in equation (1):

$$f_{\mathrm{pON}} = \frac{(R_{\mathrm{ambient}} - R_{\mathrm{NH_4NO_3}})(1+R_{\mathrm{pON}})}{(R_{\mathrm{pON}} - R_{\mathrm{NH_4NO_3}})(1+R_{\mathrm{ambient}})} \quad (1)$$

https://doi.org/10.5194/egusphere-2025-2667
Preprint. Discussion started: 7 July 2025

Where f_{pON} is the estimated fraction between the pON mass concentration and the total HR-AMS measured NO_3, and R_{ambient}, $R_{NH_4NO_3}$, and R_{pON} are the ratios between NO_2^+ and NO^+ for ambient, pure NH_4NO_3, and pure pON (determined as 2.75), respectively.

The source apportionment analysis of OA was performed on the high-resolution OA mass spectral matrix for m/z 12–120 in V mode from the HR-AMS using the PMF Evaluation Tool (PET) (Ulbrich et al., 2009). Though a Biomass Burning (BB) event was observed on the evening of July 20th (presented in the time-series results in Figure 2), it only lasted for few hours and the unconstrained PMF analysis is unable to derive a distinct BB factor for this event. To avoid biasing the PMF solution, results from this period were excluded from the PMF analysis in this study. All factors exhibited distinct temporal and spectral characteristics until a six factor, and the spectra of the six factors were consistent with source spectra in the AMS spectral database (Jeon et al., 2023). Therefore, a six-factor solution with $f_{peak} = 0$ was chosen as the optimal solution.

2.2.2 Aethalometer

The particulate matter with aerodynamic diameter less than 1 μm (PM_1) aerosol optical absorption coefficient (units of Mm^{-1} = 10^{-6} m^{-1}) at seven different wavelengths (370, 470, 520, 590, 660, and 880 and 950 nm) was measured by a dual-spot aethalometer (AE33, Magee Sci.) (Drinovec et al., 2015) at the PortablE Gas and Aerosol Sampling UnitS (PEGASUS) mobile platform (Formenti et al., 2025). The AE33 measures the light attenuation coefficient (σ_{atn}) through a filter tape, which was sampled at 1-minute intervals with a flow rate of 5 L min^{-1}. The spectral aerosol absorption coefficient is determined as:

$$\sigma_{\text{abs}} = \frac{\sigma_{\text{atn}}}{C_{\text{ref}}} \qquad (2)$$

Where C_{ref} is the multiple scattering correction factor. While the filter-based AE33 quantifies σ_{abs} via transmittance attenuation from deposited particles, its accuracy is compromised by multi-scattering interactions within the filter matrix, including variable aerosol loading and filter leakage (Yus-Díez et al., 2021). A wavelength-independent C_{ref} of 3.38 has been applied to correct the final absorption coefficient results, and more details about the corrections of AE33 results during the ACROSS campaign are presented in Di Antonio et al. (2024) and Di Antonio et al. (2025). The light absorbing equivalent Black Carbon (eBC) mass concentration is derived from the multiple scattering corrected 880 nm channel results using a mass absorption cross section (MAC) of 7.77 m^2/g (Petzold et al., 2013; Bond et al., 2013). Due to anomalous peaks at 370 nm were observed when fresh filter tape was brought into the analytical airflow during the experiments, the results from 370 nm were excluded from this study, while other wavelengths remained unaffected.

To determine the absorption contributed by the BrC, firstly, the Absorption Ångström exponent (AAE) is calculated through:

$$AAE_{\lambda_1/\lambda_2} = -\frac{\ln(\sigma_{\text{abs},\lambda_1}/\sigma_{\text{abs},\lambda_2})}{\ln(\lambda_1/\lambda_2)} \qquad (3)$$

https://doi.org/10.5194/egusphere-2025-2667
Preprint. Discussion started: 7 July 2025

Where $\sigma_{\mathrm{abs},\boldsymbol{\lambda_1}}$ and $\sigma_{abs,\boldsymbol{\lambda_2}}$ represent the absorption coefficient measured at wavelengths λ_1 (470 nm) and λ_2 (880 nm), respectively. The BrC absorption coefficient is determined in the assumption that absorption at 880 nm is contributed by BC only and the AAE for BC is 1. Henceforth, the σ_{abs} contributed by BC at 470 nm can be derived as:

$$\sigma_{abs\ \mathrm{BC},470} = \sigma_{\mathrm{abs},880\mathrm{nm}} \cdot \left(\frac{470}{880}\right)^{-AAE_{470/880}} \quad (4)$$

Then the σ_{abs} of BrC at 470 nm can be estimated as:

$$\sigma_{\mathrm{abs\ BrC},470} = \sigma_{\mathrm{abs},470} - \sigma_{abs\ \mathrm{BC},470} \quad (5)$$

2.2.3 Total PM_1 mass concentration calculation

The total PM_1 mass concentration was determined as the sum of the NR-PM_1 and eBC mass concentration measured by the HR-AMS and the AE-33, respectively.

2.3 Gas phase measurements

The nitrogen oxides (NO_x, NO_x = NO + NO_2) and total gas-phase nitrogen species (NO_y) concentrations were measured by the MPIC thermal dissociation cavity ringdown spectroscopy (TD-CRD) instrument at 405 nm (Friedrich et al., 2020), and more details about the operations of the MPIC TD-CRD during ACROSS project are described in Andersen et al. (2024). NO_2 concentration was measured by a cavity attenuated phase shift (CAPS). The O_3 and CO concentrations were measured using a commercial monitor (HORIBA APOA-370) and a CRD (Picarro) at PEGASUS platform, respectively. The VOCs were characterised through the Proton Transfer Reaction Time-of-Flight Mass Spectrometer (PTR-MS, KORE Inc.) that uses H_3O^+ as the ionization source. The PTR-MS was calibrated using the VOC standards every three days. OH radicals were measured through the Chemical Ionisation Mass Spectrometry (CIMS, LPC2E) (Kukui et al., 2008).

2.4 Other supporting measurements

Ambient air temperature and RH at near-ground level were measured using a temperature sensor (Atexis, PT1000) and a humidity sensor (Vaisala, HMP45A), respectively. The surface downwelling shortwave radiation and wind parameters were measured by a net radiometer (Kipp & Zonen, CNR4: 192119) and a wind monitor (Young, 05103: 4655) mounted on the tower.

2.5 Relative photochemical age estimation

To evaluate the impacts of photochemical reactions on secondary aerosols, relative photochemical age (t_{photo}) is estimated through the ratio between NO_x and NO_y following the method described by Nault et al. (2018):

$$t_{\mathrm{photo}} = \frac{\ln\left(\frac{[\mathrm{NO_x}]}{[\mathrm{NO_y}]}\right)}{k_{\mathrm{OH+NO_2}}[\mathrm{OH}]_{\mathrm{avg}}} \quad (6)$$

https://doi.org/10.5194/egusphere-2025-2667
Preprint. Discussion started: 7 July 2025

Where $[NO_x]$ and $[NO_y]$ are the measured concentrations of NO_x and NO_y, respectively, $[OH]_{avg}$ is the average measured OH concentration during the campaign period, which is 1.6×10^6 molecules cm^{-3}. k_{OH+NO_2} is the rate coefficient of OH with NO_2 and is assumed to be 9.2×10^{-12} cm^3 $molecules^{-1}$ s^{-1} (Mollner et al., 2010). The estimated t_{photo} was constrained to the period of 6:00 – 20:00 European Summer Time (EST) according to the diurnal trend of the radiation intensity (presented in Figure 3(a) and 3(e)). As shown in Figure 3(a) and 3(g), the diurnal trend of t_{photo} was similar to the observed OH concentration and radiation intensity diurnal trend, reinforcing its robustness as a photochemical indicator. Here, we report the calculation result as 'relative photochemical age' since the potential short lifetime of NO_y in the forest (Andersen et al., 2024) may compromise the accuracy of absolute photochemical age calculation. Only the calculated t_{photo} within 1 day (24 hours) was used here to reduce the uncertainty of the estimated t_{photo} due to the potential short lifetime of HNO_3 and other oxidised reservoirs via deposition in the forest (Nguyen et al., 2015; Romer et al., 2016).

2.6 UK Met Office NAME dispersion model

Potential source regions are identified using airmass historic results generated by the UK Met Office Numerical Atmospheric-dispersion Modelling Environment (NAME) dispersion model (Jones et al., 2007). The model calculates the integrated historical air mass contribution over 24 hours by back-tracking tracer particles (released at 1 g s^{-1} from the sampling site) on a 0.25° × 0.25° horizontal grid within the boundary layer every four hours. The model distinguishes between air masses primarily influenced by local sources and those transported regionally from broader areas. The potential airmass sources are classified into five main regions (presented in Figure 1(a)) according to the CAMS EAC4 (ECMWF Atmospheric Composition Reanalysis 4) global reanalysis PM_1 spatial distribution results (presented in Figure 1(b)) (Inness et al., 2019) during the campaign period: (1) The Ile-de-France region (IDF (local), 48° – 50° N, 1° - 3° E) represents the local emission from the Paris region; (2) The Northeast (NE) region (50°–54°N, 1°–10°E) is identified as a source of anthropogenic polluted continental air masses, evidenced by significantly elevated PM_1 concentrations in this area; (3) The Northwest (NW) region (50° – 54° N, -5° - 1° E) represents the source of polluted maritime air masses originating from the English Channel and the United Kingdom (UK); (4) The Southwest (SW) region (44° – 50° N, -5° - 3° E, exclude the IDF region) is characterized as a source of low-pollution maritime air masses, as evidenced by persistently low PM_1 concentrations over Southwest France despite several wildfire activities (the spatial distribution of fire points information during the experiment period is presented in Figure S2); and (5) The Southeast (SE) region (44° – 48° N, 3° - 10° E) represents another source of polluted continental air mass due to the high PM_1 concentration over Southeast France and North Italy. The air mass examples are presented in Figure S1 in the supplementary.

https://doi.org/10.5194/egusphere-2025-2667
Preprint. Discussion started: 7 July 2025

3. Results and discussions

3.1 Overview of meteorology and campaign conditions

Figure 2(a) presents the time series of temperature and RH, PM_1 composition, and the fractional contributions of different air masses throughout the whole campaign period. The average mass concentrations of PM_1 species and the normalised OA under different airmass dominated periods are displayed in Figure 2(b) and (c). The OA was normalised to eBC to avoid the effects of dilution during the transport. While the contribution from the local emissions (IDF air mass) was significant, external air masses also had a substantial impact on PM_1 mass concentrations. The SE airmass-dominated period was excluded from further analysis due to its short duration during the campaign. The NE airmasses brought higher average aerosol mass loadings compared to the other sectors, in agreement with the previous summertime studies in Paris, indicating that the continental airmass is generally more polluted (Crippa et al., 2013). The continental air masses also typically resulted in the highest temperatures and the lowest RH. In contrast, air masses originating from oceanic influence, whether from the SW or NW sectors, resulted in lower aerosol loadings in the Paris region, while higher RH and lower temperatures prevailed. The ECMWF CAMS reanalysis shows higher average PM_1 concentrations over the Southwest France due to the forest fires burning during the summer of 2022 (Menut et al., 2023). Although an in-situ PM_1 mass concentration spike occurred on the evening of 20 July when the SW airmass dominated, measurement data and back-dispersion analysis confirm that BB particulates from Southwest France were absent at the site for the rest of the study.

Figure 3 presents the diurnal variations of the t_{photo}, CO concentration, eBC mass concentration, temperature, downward shortwave radiation, RH, OH and NO_x concentrations under the different external airmasses dominated periods. The BB event on the evening of July 20th was excluded from the analysis. Based on the diurnal trends in meteorological parameters, increases in radiation intensity during the day were inversely correlated with decreases in RH, which reached its lowest level in the late afternoon. Due to the weaker radiation intensity or the potential shorter transport distance, the average t_{photo} and OH concentration of the SW airmass dominated period were lower compared to the other air masses dominated periods. Since the measurements were conducted away from urban emission sources, the diurnal average eBC mass concentration was with no discernible peak during rush hours, and there was only limited increase in NO_x concentrations during the morning rush hours during NE and NW periods. The daytime decrease of CO concentration during NW and SW periods was due to boundary layer dilution, with lowest CO concentrations at midday. In contrast, the NE period showed no diurnal variation of CO, suggesting the accumulation of regionally transported pollutants from surrounding areas at the suburban forest site.

https://doi.org/10.5194/egusphere-2025-2667
Preprint. Discussion started: 7 July 2025

3.2 Source apportionment of organic aerosols

Figure 4 presents the results of the PMF reanalysis conducted on the AMS observations between June 29th to July 20th, 2022, which resolved six factors: one Hydrocarbon-like OA (HOA) and five OOA factors. The person correlation coefficient (r) between the HR-AMS PMF factors and the external tracers is presented in Figure S9 in the supplementary. Figure 5 shows the diurnal variations of the OA factors, and Figure 6 presents the mass fractions of the OA factors according to air mass origins. The OOA factors accounted for over 90% of total OA during the campaign, contributing a larger mass fraction than in previous studies conducted in the Paris urban area or its environs (Crippa et al., 2013; Petit et al., 2015; Zhang et al., 2019). As expected, the HOA factor has the lowest O:C ratio (0.15) and the highest fraction of C_xH_y fragments, notably at m/z 41, 43, 55, and 57. Temporal variability shows sporadic enhancements associated with occasional vehicular activity in the vicinity of the site. However, HOA only exhibited moderate correlation with eBC (r = 0.55) and with NO_x (r = 0.49). This may be due to the remote location of the measurement site, primary anthropogenic emission sources were limited near the site.

LO-OOA1 and LO-OOA2 exhibited very similar mass spectral profiles but distinct temporal patterns, with LO-OOA1 peaking during the daytime and LO-OOA2 during the nighttime. The correlation analysis indicates that they were associated with secondary formation from biogenic precursors: while LO-OOA1 exhibited some correlation with isoprene (r = 0.43), LO-OOA2 correlated more strongly with monoterpene (r = 0.79). Since monoterpenes emitted from local vegetation can form SOA through ozonolysis, OH- or NO_3- initiated reactions at night (Lee et al., 2016), this explains the nighttime peak of LO-OOA2. Good correlation was also observed between these two OOA factors and the sum of methyl vinyl ketone (MVK) and methacrolein (MACR). Isoprene epoxydiols (IEPOX)-OOA was not identified through the HR-AMS results during the experiment period, as the mass spectral profiles of both LO-OOA1 and LO-OOA2 lacked the characteristic enhancement at m/z 82, a known tracer signal for IEPOX-OOA (Hu et al., 2015). However, both OOAs exhibited pronounced contributions at m/z 91.05, attributed to $C_7H_7^+$ fragments likely from thermal decomposition of dimers and oligomers on the vaporizer (Riva et al., 2016). These two biogenic-related LO-OOA factors contributed approximately 40% to 50% of the total OA mass concentration throughout the campaign period.

The diurnal trend shows that the LO-OOA3 concentration started increasing from the evening at around 8 pm and reached the peak in the early morning (between 6 and 8 am). The moderate positive correlation between LO-OOA3 and RH (r = 0.45) and Chl (r = 0.4) suggested that this oxygenated organic aerosol factor may be linked to marine emission sources. This is further supported by the higher mass fraction of LO-OOA3 during the marine air mass-dominated periods (SW and NW periods) compared to the continental air mass-dominated period (NE period) shown in Figure 6. The highest N:C ratio among all the OOA factors for LO-OOA3 was observed suggesting that LO-OOA3 importantly contributed to the nitrogen-containing organics. However, the correlation between LO-OOA3 and pON was poor (r = 0.06). The mass spectral profile

https://doi.org/10.5194/egusphere-2025-2667
Preprint. Discussion started: 7 July 2025

shows that the most abundant nitrogen-containing fragments were CHN^+ (m/z 27.01) and CH_4N^+ (m/z 30.03), which together contributed approximately 6% to the total LO-OOA3 signal. The presence of CH_4N^+ suggested that LO-OOA3 likely contained a contribution of reduced-N compounds such as organic amines (Ge et al., 2024). The LO-OOA3 likely originated from aqueous-phase chemistry under marine air mass dominance, where elevated RH (> 80%) at night-time promoted partitioning of nitrogen-containing organics into hygroscopic aerosol phases. Chen et al. (2019) also shows that the high RH condition promoted the formation of organic amines particles. At this suburban forest site, reduced nocturnal oxidant levels, especially during SW air mass periods, facilitated the accumulation of nitrogen-enriched LO-OOA3. In contrast, daytime photo-oxidation driven by OH radicals and secondary oxidants (e.g., O_3) effectively degraded LO-OOA3, as evidenced by strong inverse correlations between LO-OOA3 and photochemical-relate OVOCs (e.g. with MVK+MACR: r = -0.69).

LO-OOA4 exhibited a good correlation with sulfate (r = 0.67) and moderate correlation with inorganic nitrate (r = 0.42). The wind rose analysis (shown in Figure S8 in the supplementary) reveals that LO-OOA4 predominantly originated from anthropogenic polluted air masses advected from the NE and NW regions. Consequently, during the SW period, LO-OOA4 contributed only 6% to the total OA mass concentration. In contrast, its contribution increased to 15% and 13% with the increasing pollution level during the NW and NE periods, respectively.

The MO-OOA was with the highest average O:C ratio (0.86) among all the factors, and dominant peaks were presented at m/z 28 (CO^+) and 44 (CO_2^+). The significant increase in MO-OOA observed during the afternoon, despite boundary layer dilution, indicates that summertime MO-OOA formation was strongly driven by active photochemical processes. Due to the reduction of photochemical activity during the SW period, the mass fraction of MO-OOA during the SW period was smaller than the fraction during the other periods. The wind rose analysis shows that the MO-OOA was contributed significantly from the anthropogenic polluted NE regions.

3.3 Evolution of aerosol compositions due to photochemical aging

Figure 7 illustrates the evolution of O_x (O_3 + NO_2) mixing ratio, O:C ratio, and NR-PM_1 components concentrations normalised to eBC as a function of t_{photo}. The results are averaged into four-hour intervals along t_{photo} to illustrate their evolution. To quantify the relative photochemical-age-dependent evolution of particulate phase components, an exponential fitting was applied to the factors that showed significant correlation with t_{photo}:

$$y = A \cdot \exp(B \cdot t_{photo}) \quad (7)$$

Where the coefficient B quantifies the relative hourly change rate of each factor. As discussed previously in Section 2.5, the absolute photochemical age calculation may be with certain uncertainties. Therefore, the hourly change rate reported in this

https://doi.org/10.5194/egusphere-2025-2667
Preprint. Discussion started: 7 July 2025

study was used to assess the relative variations in parameters. The fitting results are summarized in Table S1. The uncertainty of coefficient B, reported as its standard deviation, reflects the variability inherent to the regression analysis.

The correlation between t_{photo} and O_x concentrations shown in Figure 7(a) indicate that the photochemical process in summer has a significant impact on the formation of O_x throughout the experiment period. This agrees with the previous study in Beijing during summertime (Chen et al., 2021) and suggests that increased photochemical aging leads to greater consumption of VOCs, which in turn accelerates NO_x cycling and promotes the accumulation of tropospheric O_3. The NE period showed higher average O_x concentrations compared to the NW and SW periods during the relative ~24-hour photochemical aging period.

The normalised PM_1 concentration, shown in Figure 7(b) as a function of t_{photo}, exhibited a consistent increase across all three periods with higher t_{photo}, and the normalised OA mass concentration doubled following a relative ~24-hour photochemical aging process as presented in Figure 7(c). The relative increasing rate of PM_1 was 3.8 ($\pm$ 0.5) % h^{-1}, 2.5 ($\pm$ 0.3) % h^{-1}, and 2.9 ($\pm$ 0.7) % h^{-1} for SW, NW and NE periods, respectively. While the relative production rate of OA was higher which was 5.0 ($\pm$ 0.5) % h^{-1}, 3.5 ($\pm$ 0.3) % h^{-1}, and 3.7 ($\pm$ 1.0) % h^{-1} for SW, NW and NE periods, respectively. This higher OA production rate compared to the average PM_1 production rate indicates that photochemical formation of OA played a significant role in the increase of total PM_1 concentration following relative ~24 hours of photochemical aging. This finding aligns with previous studies in Europe, which have shown that OOA formation substantially contributes to summer PM_1 levels (Chen et al., 2022; Zhang et al., 2019). The increasing trend of OA also agreed with the results previously observed in urban plumes from Paris, Mexico City, and Seoul (Freney et al., 2014; Decarlo et al., 2010; Nault et al., 2018) during photochemical process. However, the average bulk O:C ratio did not show a corresponding increase with t_{photo}; instead, a slight decrease was observed at higher t_{photo}, particularly during the NE dominated period. The high average bulk O:C ratio at the initial point suggests that the OA was already highly oxidized at t_{photo} = 0. Subsequent contribution of additional LO-OOA from photochemical process may have diluted the overall oxidation level, leading to a decrease in the average bulk O:C ratio.

The sulfate concentrations exhibited minimal variation with t_{photo} here, regardless of the period, likely due to the limited availability of SO_2 precursors in the Rambouillet remote measurement site. Previous studies have demonstrated rapid conversion of SO_2 into sulfate via aging processes in urban areas (Wu et al., 2022; Chen et al., 2021) or near emission sources (Yu et al., 2020). Concerning particulate nitrate, which on average during the experiment period was over 80% attributed to pON, has shown distinct behaviours between its inorganic and organic fractions. For inorganic nitrate compounds, concentrations in the NW and SW period slightly decreased with increasing t_{photo}, whereas those in the NE period exhibited a minor increasing trend. It is likely that this variation was due to the availability of NO_x concentrations

https://doi.org/10.5194/egusphere-2025-2667
Preprint. Discussion started: 7 July 2025

during different periods. The SW period showed a slight increase in the pON concentration with t_{photo} increases, while the NE and NW periods displayed a decreasing trend. This difference was due to depletion of primary pON and concurrent formation of secondary pON during photochemical aging, and this relationship will be further explored through linking to the trend of PMF-derived factors.

Figure 8 shows the evolution of normalised concentrations of HR-AMS PMF-derived factors and gas phase components measured by PTR-MS. For consistency, primary anthropogenic VOCs (Toluene + Benzene) were normalised against ΔCO to account for dilution. The evolution of absolute particulate and gas-phase concentrations is presented in Figure S10 in the supplementary. For the primary OA compounds, the HOA shown a decreasing trend with the increase of t_{photo} during the NE and NW periods. Same decreasing trend was also observed for the primary anthropogenic VOCs (Toluene + Benzene). During the SW period, HOA concentrations exhibited a slight increase, and the Toluene + Benzene concentrations remained independent of t_{photo}. Previous studies in the polluted urban areas have shown that strong photochemical processes lead to the oxidation of the HOA and traffic related primary VOCs (Wu et al., 2022; Chen et al., 2021). However, reduced radiation levels decreased the photochemical oxidation rate of primary traffic-related pollutants, potentially leading to their accumulation in suburban forested areas. As HOA has shown some correlation with the pON (r = 0.35), this may explain that the decline in pON concentration with t_{photo} was driven by photodepletion of primary pON during intense photochemical activity, while the photo loss of primary pON during the SW period was slower than the other periods.

Due to the increase emission of isoprene as a function of t_{photo} (shown in Figure 8(h)), the biogenic-related LO-OOA1 and LO-OOA2 also showed an increasing trend during all the three periods. All the periods illustrated a close relative production rate of around for LO-OOA1 which is 8.0 (± 2.0) % h^{-1}, 8.1 (± 2.0) % h^{-1} and 6.6 (± 3.0) % h^{-1} for SW, NW, and NE period, respectively. However, for the LO-OOA2, the relative increasing rates were slower compared to LO-OOA1 and were 5.3 (± 2.7) % h^{-1}, 4.3 (± 2) % h^{-1}, and 2.6 (± 0.5) % h^{-1} for SW, NW, and NE period, respectively. Moreover, LO-OOA2 did not show a strong correlation with t_{photo} during the NE period. As discussed in Section 3.2, LO-OOA2 can likely be attributed to SOA formation from locally emitted monoterpenes. Therefore, the variation of LO-OOA2 may also be significantly influenced by other factors, such as changes in boundary layer height (BLH), which affect the accumulation or dispersion of local vegetation emissions.

During the NE period, LO-OOA3 exhibited a clear decreasing trend with increasing t_{photo} at a relative rate of -2.9 (± 1.4) % h^{-1}, whereas no distinct trend was observed in the other periods. Elevated OH radical and secondary oxidant concentrations during the NE period likely enhanced oxidative depletion of nitrogen-enriched LO-OOA3 relative to other periods. While continental pollution-related LO-OOA4 demonstrated a strong dependence on photochemical processes, its variability may also be influenced by dominant air masses, as the SW period was with lower average normalised mass concentrations

https://doi.org/10.5194/egusphere-2025-2667
Preprint. Discussion started: 7 July 2025

compared to other periods. The MO-OOA showed strong correlation with the photochemical process. The relative production rates for the NE and NW periods were 6.4 (± 1.3) % h^{-1}, 6.4 (± 1.5) % h^{-1}, and they were higher than the relative production rate during the SW periods (4.8 (± 2.1) % h^{-1}). The normalised mass concentrations of MO-OOA during the NE and NW period were significantly higher than the concentration during the SW period after a relative ~24-hour photochemical aging. Limited formation of MO-OOA during the SW period led to a lower average bulk O:C ratio compared to other periods. Moreover, our findings indicate that highly oxidized particulate species were not favoured under conditions of low radiation and high relative humidity. In addition, LO-OOA4 and MO-OOA also exhibited a correlation with pON (r = 0.34 and 0.3, respectively), suggesting that LO-OOA4 and MO-OOA importantly contributed to secondary pON formation during photochemical aging. Thereby, the concurrent depletion of HOA and formation of LO-OOA4 and MO-OOA likely govern the observed variations in total pON concentrations throughout the photochemical aging process.

3.4 The impact of photochemical aging on aerosol optical properties

Figure 9 illustrates the increasing contribution of BrC to the total aerosol light absorption coefficient at 470 nm as a function of t_{photo}, particularly during the NE and NW periods. As t_{photo} increased from around 2 hours to nearly 24 hours, the average BrC absorption fraction rose from about 17% to 23% in the NE period and from roughly 18% to 26% in the NW period. To identify and quantify the contribution of different OA factors to the total $\sigma_{\mathrm{abs\ BrC,470}}$, a Multiple Linear Regression (MLR) analysis was applied using the OA factors from the PMF analysis during the whole experiment period (with BB period removed). The *p*-test ($p < 0.01$) was also applied to assess the statistical significance of each parameter. The MLR relationship between $\sigma_{\mathrm{abs\ BrC,470}}$ and PMF-derived factors are formulated as:

$$\sigma_{\mathrm{abs\ BrC,470}} = a_0 + \sum_i a_i\,[C_i] \qquad (8)$$

Where a_0 represents the intercept, and a_i represents the regression coefficient for each PMF-derived factor C_i. These regression coefficients can be associated with the Mass Absorption Coefficients (MAC) of each PMF-derived factor.

Table 1 presents the results of the regression factors of the MLR analysis between $\sigma_{\mathrm{abs\ BrC,470}}$ and PMF-derived factors. The correlation coefficient is also presented to illustrate the contribution of each PMF-derived factor to the total BrC absorption during the whole experiment period. Interestingly, the LO-OOA3 and MO-OOA, which have the highest nitrogen content among all factors, also depict high MAC (regression coefficients). Nonetheless, their correlations with BrC differ markedly: LO-OOA3 displayed a significant negative partial correlation, whereas MO-OOA was strongly positively correlated. The HOA and LO-OOA4 also showed high MAC which were 0.47 $m^2\ g^{-1}$ and 0.30 $m^2\ g^{-1}$, respectively, and they exhibited fair correlation with BrC. It is interesting to note that HOA, LO-OOA4 and MO-OOA also exhibited correlation with the pON, typically associated as an important component of BrC (Laskin et al., 2015)

https://doi.org/10.5194/egusphere-2025-2667
Preprint. Discussion started: 7 July 2025

Combined with the photochemical aging process discussed in Section 3.3, the decline in HOA concentration with photochemical aging during the NE and NW period demonstrated a reduced contribution of primary BrC following a relative ~24-hour photochemical aging process. The photochemical process also suppressed the formation of LO-OOA3 or oxidized it into MO-OOA, particularly during the NE period. Conversely, the increase in BrC absorption fraction as a function of t_{photo} highlighted the production of more secondary BrC. This suggested that photochemical aging-driven formation of MO-OOA dominated the contribution to enhancement of the overall BrC absorption contribution at short wavelength, particularly during high solar radiation periods (NE and NW periods) in summer. Previous studies also demonstrated that the photochemical process promoted the enhancement of the secondary BrC absorption in urban (Li et al., 2023) and remote areas (Wu et al., 2024). The persistence of secondary BrC in remote regions demonstrated their enhanced summertime production efficiency, thus amplifying their direct radiative effects through solar radiation interactions. The weak absorption capacity of LO-OOA1 and LO-OOA2 suggested that these PMF-derived factors exhibited negligible short-wavelength absorption. While LO-OOA1 and LO-OOA2 were predominantly associated with Biogenic SOA (BSOA) derived from isoprene and monoterpene oxidation, they typically displayed limited light absorption properties due to the prevalence of non-chromophoric oxygenated products (Flores et al., 2014; Laskin et al., 2015).

Conclusions

In this paper, we present a study in a suburban forest region of a European megacity in summer to demonstrate the impacts of photochemical process on aerosol properties in a mixed anthropogenic and biogenic environment. Based on the detailed mass spectra of the HR-AMS, we resolved primary and secondary OA sources via PMF analysis, enabling quantitative tracking of the evolution of OA during photochemical aging. OA was found to dominate the total aerosol mass concentrations during the whole experiment period and strongly correlated with the photochemical aging. The observed increasing trend in OA with relative photochemical age was primarily driven by the production of OOA, sourced from both biogenic and anthropogenic precursors. The production rate of different types of OOA was found to vary with the geographical origin of the air masses: the NE continental air mass introduced higher average PM pollution levels to the Paris region, coupled with dry conditions and strong solar radiation, whereas the SW marine air mass resulted in lower pollution levels and wet, low-radiation meteorological conditions. OOA formed during the SW period exhibited a lower oxidation state (indicated by a reduced average bulk O:C ratio) compared to other periods, with nitrogen-enriched LO-OOA contributing a significantly higher proportion to total OA during this time. In contrast, intense photochemical activity during the NE period drove substantial MO-OOA formation. During the NE period, although photochemical depletion of primary anthropogenic OA and nitrogen-enriched LO-OOA occurred, this was offset by rapid formation of MO-OOA and subsequent secondary BrC production, leading to an increasing fraction of total BrC at shorter wavelengths with relative photochemical age. This result reveals that formation of secondary BrC from photochemical process dominated the contribution to the total light-absorbing OA in a mixed anthropogenic and biogenic environment during the heatwave in summertime. This highlights the critical need to incorporate BrC formation mechanisms into models to accurately simulate direct radiative effect (Drugé

https://doi.org/10.5194/egusphere-2025-2667
Preprint. Discussion started: 7 July 2025

et al., 2022). In addition to the impacts on the aerosol optical properties, photochemical processes can drive particle growth via the partitioning of semi-volatile organic compounds (Zaveri et al., 2022) and enhance particle hygroscopicity (Wang et al., 2018), thus affecting the CCN activity. Furthermore, photochemical-driven OOA formation during summer may pose significant human health risks by contributing to PM-induced oxidative stress (Tuet et al., 2017; Tuet et al., 2016).

Author Contribution

CC and VM designed the ACROSS Rambouillet experiments; CY performed the data analysis and wrote the paper; PF provided guidance with the analysis and writing; CY, PF, JB, CDB, LDA, TS, STA, PD, GNTET, JNC, AK, CX, CD, MCi, MCa, CC and VM performed experiments; JB performed the operation and data analysis of the HR-AMS; CY and JB performed the HR-AMS PMF analysis; CDB and LDA performed the operation and data analysis of AE33; TS, STA, PD, GNTET and JNC performed the operation and data analysis of TD-CRD; AK and CX performed the operation and data analysis of CIMS; CD, OG and JCE performed the operation and data analysis of the meteorological data measurements; VM, HB, and AB performed the operation and data analysis of PTR-MS; CY and HW performed the back dispersion analysis of UK Met Office NAME dispersion model; CG coordinate the technical aspect of the Rambouillet experiments; FM, MCa, ABe and PZ contributed to the design and preparation of measurement infrastructures at the Rambouillet site; JDA, DL and YW contributed to the data analysis and discussions.

Acknowledgment

Authors are grateful to the ACROSS consortium for their work prior and during the field campaign. The authors wish to thank AERIS (https://www.aeris-data.fr/), the French centre for atmospheric data and service, for providing the campaign website and organizing the curation and open distribution of the ACROSS data. Chenjie Yu would like to acknowledge the European Union Marie Skłodowska-Curie COFUND Postdoctoral Fellowship program supported by the Paris Region. Special thanks to Benjamin A. Nault and Peter F. DeCarlo (Johns Hopkins University) for their valuable discussions and suggestions contributing to this study.

Financial support

The ACROSS project has received funding from the French National Research Agency (ANR), with the reference ANR-20-CE01-0010, and under the investment program integrated into France 2030, with the reference ANR–17–MPGA–0002, and it was supported by the French National program LEFE (Les Enveloppes Fluides et l'Environnement) of the CNRS/INSU (Centre National de la Recherche Scientifique/Institut National des Sciences de L'Univers). This research also receives funding from the European Union's Horizon 2020 research and innovation programme under the Marie Skłodowska-Curie grant agreement n° 945298. The PEGASUS facility receives funding as a national facility (instrument national) of the CNRS INSU. The French State under the France-2030 programme and the

https://doi.org/10.5194/egusphere-2025-2667
Preprint. Discussion started: 7 July 2025

Initiative of Excellence of the University of Lille are acknowledged for the funding and support granted to the R-CDP-24-003-AREA project.

Data availability

The below-canopy measurement data for Ramouillet site measurements during ACROSS project is available from the AERIES website (https://across.aeris-data.fr/, last access: 01/04/2025): which includes NR-PM1 data from HR-AMS (Brito and Riffault, 2023), NO_x, NO_y and O_3 data (Crowley, 2024). OH data from CIMS (Kukui, 2023), eBC and multi-wavelength absorption data from AE33 (Di Antonio and Di Biagio, 2024), VOC data from LISA PTR-MS data (Michoud and Bouzidi, 2024), and meteorological data (Denjean, 2023).

References

Allan, J. D., Williams, P. I., Morgan, W. T., Martin, C. L., Flynn, M. J., Lee, J., Nemitz, E., Phillips, G. J., Gallagher, M. W., and Coe, H.: Contributions from transport, solid fuel burning and cooking to primary organic aerosols in two UK cities, Atmos. Chem. Phys., 10, 647-668, 10.5194/acp-10-647-2010, 2010.

Andersen, S. T., McGillen, M. R., Xue, C., Seubert, T., Dewald, P., Türk, G. N. T. E., Schuladen, J., Denjean, C., Etienne, J. C., Garrouste, O., Jamar, M., Harb, S., Cirtog, M., Michoud, V., Cazaunau, M., Bergé, A., Cantrell, C., Dusanter, S., Picquet-Varrault, B., Kukui, A., Mellouki, A., Carpenter, L. J., Lelieveld, J., and Crowley, J. N.: Measurement report: Sources, sinks, and lifetime of NOx in a suburban temperate forest at night, Atmos. Chem. Phys., 24, 11603-11618, 10.5194/acp-24-11603-2024, 2024.

Beekmann, M., Prévôt, A. S. H., Drewnick, F., Sciare, J., Pandis, S. N., Denier van der Gon, H. A. C., Crippa, M., Freutel, F., Poulain, L., Ghersi, V., Rodriguez, E., Beirle, S., Zotter, P., von der Weiden-Reinmüller, S. L., Bressi, M., Fountoukis, C., Petetin, H., Szidat, S., Schneider, J., Rosso, A., El Haddad, I., Megaritis, A., Zhang, Q. J., Michoud, V., Slowik, J. G., Moukhtar, S., Kolmonen, P., Stohl, A., Eckhardt, S., Borbon, A., Gros, V., Marchand, N., Jaffrezo, J. L., Schwarzenboeck, A., Colomb, A., Wiedensohler, A., Borrmann, S., Lawrence, M., Baklanov, A., and Baltensperger, U.: In situ, satellite measurement and model evidence on the dominant regional contribution to fine particulate matter levels in the Paris megacity, Atmos. Chem. Phys., 15, 9577-9591, 10.5194/acp-15-9577-2015, 2015.

Bond, T. C., Doherty, S. J., Fahey, D. W., Forster, P. M., Berntsen, T., DeAngelo, B. J., Flanner, M. G., Ghan, S., Kärcher, B., Koch, D., Kinne, S., Kondo, Y., Quinn, P. K., Sarofim, M. C., Schultz, M. G., Schulz, M., Venkataraman, C., Zhang, H., Zhang, S., Bellouin, N., Guttikunda, S. K., Hopke, P. K., Jacobson, M. Z., Kaiser, J. W., Klimont, Z., Lohmann, U., Schwarz, J. P., Shindell, D., Storelvmo, T., Warren, S. G., and Zender, C. S.: Bounding the role of black carbon in the climate system: A scientific assessment, Journal of Geophysical Research: Atmospheres, 118, 5380-5552, https://doi.org/10.1002/jgrd.50171, 2013.

Bressi, M., Sciare, J., Ghersi, V., Bonnaire, N., Nicolas, J. B., Petit, J. E., Moukhtar, S., Rosso, A., Mihalopoulos, N., and Féron, A.: A one-year comprehensive chemical characterisation of fine aerosol (PM_{2.5}) at urban, suburban and rural background sites in the region of Paris (France), Atmos. Chem. Phys., 13, 7825-7844, 10.5194/acp-13-7825-2013, 2013.

Brito, J. and Riffault, V.: ACROSS_IMTNE_RambForest_AMS_BelowCanopy_L2 [dataset], https://doi.org/10.25326/492, 2023.

Canagaratna, M. R., Jimenez, J. L., Kroll, J. H., Chen, Q., Kessler, S. H., Massoli, P., Hildebrandt Ruiz, L., Fortner, E., Williams, L. R., Wilson, K. R., Surratt, J. D., Donahue, N. M., Jayne, J. T., and Worsnop, D. R.: Elemental ratio measurements of organic compounds using aerosol mass spectrometry: characterization, improved calibration, and implications, Atmos. Chem. Phys., 15, 253-272, 10.5194/acp-15-253-2015, 2015.

https://doi.org/10.5194/egusphere-2025-2667
Preprint. Discussion started: 7 July 2025

Cantrell, C. and Michoud, V.: An Experiment to Study Atmospheric Oxidation Chemistry and Physics of Mixed Anthropogenic–Biogenic Air Masses in the Greater Paris Area, Bulletin of the American Meteorological Society, 103, 599-603, https://doi.org/10.1175/BAMS-D-21-0115.1, 2022.

Cappa, C. D., Lim, C. Y., Hagan, D. H., Coggon, M., Koss, A., Sekimoto, K., de Gouw, J., Onasch, T. B., Warneke, C., and Kroll, J. H.: Biomass-burning-derived particles from a wide variety of fuels – Part 2: Effects of photochemical aging on particle optical and chemical properties, Atmos. Chem. Phys., 20, 8511-8532, 10.5194/acp-20-8511-2020, 2020.

Chen, G., Canonaco, F., Tobler, A., Aas, W., Alastuey, A., Allan, J., Atabakhsh, S., Aurela, M., Baltensperger, U., Bougiatioti, A., De Brito, J. F., Ceburnis, D., Chazeau, B., Chebaicheb, H., Daellenbach, K. R., Ehn, M., El Haddad, I., Eleftheriadis, K., Favez, O., Flentje, H., Font, A., Fossum, K., Freney, E., Gini, M., Green, D. C., Heikkinen, L., Herrmann, H., Kalogridis, A.-C., Keernik, H., Lhotka, R., Lin, C., Lunder, C., Maasikmets, M., Manousakas, M. I., Marchand, N., Marin, C., Marmureanu, L., Mihalopoulos, N., Močnik, G., Nęcki, J., O'Dowd, C., Ovadnevaite, J., Peter, T., Petit, J.-E., Pikridas, M., Matthew Platt, S., Pokorná, P., Poulain, L., Priestman, M., Riffault, V., Rinaldi, M., Różański, K., Schwarz, J., Sciare, J., Simon, L., Skiba, A., Slowik, J. G., Sosedova, Y., Stavroulas, I., Styszko, K., Teinemaa, E., Timonen, H., Tremper, A., Vasilescu, J., Via, M., Vodička, P., Wiedensohler, A., Zografou, O., Cruz Minguillón, M., and Prévôt, A. S. H.: European aerosol phenomenology − 8: Harmonised source apportionment of organic aerosol using 22 Year-long ACSM/AMS datasets, Environment International, 166, 107325, https://doi.org/10.1016/j.envint.2022.107325, 2022.

Chen, T., Liu, J., Ma, Q., Chu, B., Zhang, P., Ma, J., Liu, Y., Zhong, C., Liu, P., Wang, Y., Mu, Y., and He, H.: Measurement report: Effects of photochemical aging on the formation and evolution of summertime secondary aerosol in Beijing, Atmos. Chem. Phys., 21, 1341-1356, 10.5194/acp-21-1341-2021, 2021.

Chen, Y., Tian, M., Huang, R. J., Shi, G., Wang, H., Peng, C., Cao, J., Wang, Q., Zhang, S., Guo, D., Zhang, L., and Yang, F.: Characterization of urban amine-containing particles in southwestern China: seasonal variation, source, and processing, Atmos. Chem. Phys., 19, 3245-3255, 10.5194/acp-19-3245-2019, 2019.

Crippa, M., El Haddad, I., Slowik, J. G., DeCarlo, P. F., Mohr, C., Heringa, M. F., Chirico, R., Marchand, N., Sciare, J., Baltensperger, U., and Prévôt, A. S. H.: Identification of marine and continental aerosol sources in Paris using high resolution aerosol mass spectrometry, Journal of Geophysical Research: Atmospheres, 118, 1950-1963, https://doi.org/10.1002/jgrd.50151, 2013.

Crowley, J.: ACROSS_MPIC_RambForest_NOx_1min_L2. [dataset], https://doi.org/10.25326/687 2024.

Day, D. A., Campuzano-Jost, P., Nault, B. A., Palm, B. B., Hu, W., Guo, H., Wooldridge, P. J., Cohen, R. C., Docherty, K. S., Huffman, J. A., de Sá, S. S., Martin, S. T., and Jimenez, J. L.: A systematic re-evaluation of methods for quantification of bulk particle-phase organic nitrates using real-time aerosol mass spectrometry, Atmos. Meas. Tech., 15, 459-483, 10.5194/amt-15-459-2022, 2022.

DeCarlo, P. F., Ulbrich, I. M., Crounse, J., de Foy, B., Dunlea, E. J., Aiken, A. C., Knapp, D., Weinheimer, A. J., Campos, T., Wennberg, P. O., and Jimenez, J. L.: Investigation of the sources and processing of organic aerosol over the Central Mexican Plateau from aircraft measurements during MILAGRO, Atmos. Chem. Phys., 10, 5257-5280, 10.5194/acp-10-5257-2010, 2010.

DeCarlo, P. F., Kimmel, J. R., Trimborn, A., Northway, M. J., Jayne, J. T., Aiken, A. C., Gonin, M., Fuhrer, K., Horvath, T., Docherty, K. S., Worsnop, D. R., and Jimenez, J. L.: Field-Deployable, High-Resolution, Time-of-Flight Aerosol Mass Spectrometer, Analytical Chemistry, 78, 8281-8289, 10.1021/ac061249n, 2006.

Denjean, C.: ACROSS_CNRM_RambForest_MTO-1MIN_L2 [dataset], https://doi.org/10.25326/437 2023.

Di Antonio, L. and Di Biagio, C.: ACROSS_LISA_RambForest_AETH-Abs_PM1_1-Min_L2-station_processed, https://doi.org/10.25326/669 2024.

Di Antonio, L., Beekmann, M., Siour, G., Michoud, V., Cantrell, C., Bauville, A., Bergé, A., Cazaunau, M., Chevaillier, S., Cirtog, M., de Brito, J. F., Formenti, P., Gaimoz, C., Garret, O., Gratien, A., Gros, V., Haeffelin, M., Hawkins, L. N., Kotthaus, S., Noyalet, G., Pereira, D., Petit, J. E., Pronovost, E. D., Riffault, V., Yu, C., Foret, G., Doussin, J. F., and Di Biagio, C.: Modelling of atmospheric variability of gas and aerosols during the ACROSS campaign 2022 in the greater Paris area: evaluation of the meteorology, dynamics and chemistry, EGUsphere, 2024, 1-40, 10.5194/egusphere-2024-2175, 2024.

Di Antonio, L., Di Biagio, C., Formenti, P., Gratien, A., Michoud, V., Cantrell, C., Bauville, A., Bergé, A., Cazaunau, M., Chevaillier, S., Cirtog, M., Coll, P., D'Anna, B., de Brito, J. F., De Haan, D. O., Dignum, J. R., Deshmukh, S., Favez, O., Flaud, P. M., Gaimoz, C., Hawkins, L. N., Kammer, J., Language, B., Maisonneuve, F., Močnik, G.,

https://doi.org/10.5194/egusphere-2025-2667
Preprint. Discussion started: 7 July 2025

Perraudin, E., Petit, J. E., Acharja, P., Poulain, L., Pouyes, P., Pronovost, E. D., Riffault, V., Roundtree, K. I., Shahin, M., Siour, G., Villenave, E., Zapf, P., Foret, G., Doussin, J. F., and Beekmann, M.: Aerosol spectral optical properties in the Paris urban area and its peri-urban and forested surroundings during summer 2022 from ACROSS surface observations, Atmos. Chem. Phys., 25, 3161-3189, 10.5194/acp-25-3161-2025, 2025.

Drinovec, L., Močnik, G., Zotter, P., Prévôt, A. S. H., Ruckstuhl, C., Coz, E., Rupakheti, M., Sciare, J., Müller, T., Wiedensohler, A., and Hansen, A. D. A.: The "dual-spot" Aethalometer: an improved measurement of aerosol black carbon with real-time loading compensation, Atmos. Meas. Tech., 8, 1965-1979, 10.5194/amt-8-1965-2015, 2015.

Drugé, T., Nabat, P., Mallet, M., Michou, M., Rémy, S., and Dubovik, O.: Modeling radiative and climatic effects of brown carbon aerosols with the ARPEGE-Climat global climate model, Atmos. Chem. Phys., 22, 12167-12205, 10.5194/acp-22-12167-2022, 2022.

Farmer, D. K., Cappa, C. D., and Kreidenweis, S. M.: Atmospheric Processes and Their Controlling Influence on Cloud Condensation Nuclei Activity, Chemical Reviews, 115, 4199-4217, 10.1021/cr5006292, 2015.

Flores, J. M., Washenfelder, R. A., Adler, G., Lee, H. J., Segev, L., Laskin, J., Laskin, A., Nizkorodov, S. A., Brown, S. S., and Rudich, Y.: Complex refractive indices in the near-ultraviolet spectral region of biogenic secondary organic aerosol aged with ammonia, Physical Chemistry Chemical Physics, 16, 10629-10642, 10.1039/C4CP01009D, 2014.

Formenti, P., Giorio, C., Desboeufs, K., Zherebker, A., Gaetani, M., Baldo, C., Landrot, G., Montebello, S., Chevaillier, S., Triquet, S., Siour, G., Di Biagio, C., Battaglia, F., Doussin, J. F., Feron, A., Namwoonde, A., and Piketh, S. J.: Elemental composition, iron mineralogy and solubility of anthropogenic and natural mineral dust aerosols in Namibia: a case study analysis from the AEROCLO-sA campaign, EGUsphere, 2025, 1-28, 10.5194/egusphere-2025-446, 2025.

Fossum, K. N., Lin, C., O'Sullivan, N., Lei, L., Hellebust, S., Ceburnis, D., Afzal, A., Tremper, A., Green, D., Jain, S., Byčenkienė, S., O'Dowd, C., Wenger, J., and Ovadnevaite, J.: Two distinct ship emission profiles for organic-sulfate source apportionment of PM in sulfur emission control areas, Atmos. Chem. Phys., 24, 10815-10831, 10.5194/acp-24-10815-2024, 2024.

Freney, E. J., Sellegri, K., Canonaco, F., Colomb, A., Borbon, A., Michoud, V., Doussin, J. F., Crumeyrolle, S., Amarouche, N., Pichon, J. M., Bourianne, T., Gomes, L., Prevot, A. S. H., Beekmann, M., and Schwarzenböeck, A.: Characterizing the impact of urban emissions on regional aerosol particles: airborne measurements during the MEGAPOLI experiment, Atmos. Chem. Phys., 14, 1397-1412, 10.5194/acp-14-1397-2014, 2014.

Friedrich, N., Tadic, I., Schuladen, J., Brooks, J., Darbyshire, E., Drewnick, F., Fischer, H., Lelieveld, J., and Crowley, J. N.: Measurement of NOx and NOy with a thermal dissociation cavity ring-down spectrometer (TD-CRDS): instrument characterisation and first deployment, Atmos. Meas. Tech., 13, 5739-5761, 10.5194/amt-13-5739-2020, 2020.

Gao, M., Zhou, S., He, Y., Zhang, G., Ma, N., Li, Y., Li, F., Yang, Y., Peng, L., Zhao, J., Bi, X., Hu, W., Sun, Y., Wang, B., and Wang, X.: In Situ Observation of Multiphase Oxidation-Driven Secondary Organic Aerosol Formation during Cloud Processing at a Mountain Site in Southern China, Environmental Science & Technology Letters, 10, 573-581, 10.1021/acs.estlett.3c00331, 2023.

Ge, X., Sun, Y., Trousdell, J., Chen, M., and Zhang, Q.: Enhancing characterization of organic nitrogen components in aerosols and droplets using high-resolution aerosol mass spectrometry, Atmospheric Measurement Techniques, 17, 423-439, 10.5194/amt-17-423-2024, 2024.

Grange, S. K., Lee, J. D., Drysdale, W. S., Lewis, A. C., Hueglin, C., Emmenegger, L., and Carslaw, D. C.: COVID-19 lockdowns highlight a risk of increasing ozone pollution in European urban areas, Atmos. Chem. Phys., 21, 4169-4185, 10.5194/acp-21-4169-2021, 2021.

Healy, R. M., Sciare, J., Poulain, L., Crippa, M., Wiedensohler, A., Prévôt, A. S. H., Baltensperger, U., Sarda-Estève, R., McGuire, M. L., Jeong, C. H., McGillicuddy, E., O'Connor, I. P., Sodeau, J. R., Evans, G. J., and Wenger, J. C.: Quantitative determination of carbonaceous particle mixing state in Paris using single-particle mass spectrometer and aerosol mass spectrometer measurements, Atmos. Chem. Phys., 13, 9479-9496, 10.5194/acp-13-9479-2013, 2013.

Hu, W. W., Campuzano-Jost, P., Palm, B. B., Day, D. A., Ortega, A. M., Hayes, P. L., Krechmer, J. E., Chen, Q., Kuwata, M., Liu, Y. J., de Sá, S. S., McKinney, K., Martin, S. T., Hu, M., Budisulistiorini, S. H., Riva, M., Surratt, J. D., St. Clair, J. M., Isaacman-Van Wertz, G., Yee, L. D., Goldstein, A. H., Carbone, S., Brito, J., Artaxo, P., de Gouw, J. A., Koss, A., Wisthaler, A., Mikoviny, T., Karl, T., Kaser, L., Jud, W., Hansel, A., Docherty, K. S., Alexander, M. L., Robinson, N. H., Coe, H., Allan, J. D., Canagaratna, M. R., Paulot, F., and Jimenez, J. L.: Characterization of a real-time tracer for

https://doi.org/10.5194/egusphere-2025-2667
Preprint. Discussion started: 7 July 2025

isoprene epoxydiols-derived secondary organic aerosol (IEPOX-SOA) from aerosol mass spectrometer measurements, Atmos. Chem. Phys., 15, 11807-11833, 10.5194/acp-15-11807-2015, 2015.

Inness, A., Ades, M., Agustí-Panareda, A., Barré, J., Benedictow, A., Blechschmidt, A. M., Dominguez, J. J., Engelen, R., Eskes, H., Flemming, J., Huijnen, V., Jones, L., Kipling, Z., Massart, S., Parrington, M., Peuch, V. H., Razinger, M., Remy, S., Schulz, M., and Suttie, M.: The CAMS reanalysis of atmospheric composition, Atmos. Chem. Phys., 19, 3515-3556, 10.5194/acp-19-3515-2019, 2019.

Jayne, J. T., Leard, D. C., Zhang, X., Davidovits, P., Smith, K. A., Kolb, C. E., and Worsnop, D. R.: Development of an Aerosol Mass Spectrometer for Size and Composition Analysis of Submicron Particles, Aerosol Science and Technology, 33, 49-70, 10.1080/027868200410840, 2000.

Jeon, S., Walker, M. J., Sueper, D. T., Day, D. A., Handschy, A. V., Jimenez, J. L., and Williams, B. J.: A searchable database and mass spectral comparison tool for the Aerosol Mass Spectrometer (AMS) and the Aerosol Chemical Speciation Monitor (ACSM), Atmos. Meas. Tech., 16, 6075-6095, 10.5194/amt-16-6075-2023, 2023.

Jiang, X., Liu, D., Li, Q., Tian, P., Wu, Y., Li, S., Hu, K., Ding, S., Bi, K., Li, R., Huang, M., Ding, D., Chen, Q., Kong, S., Li, W., Pang, Y., and He, D.: Connecting the Light Absorption of Atmospheric Organic Aerosols with Oxidation State and Polarity, Environmental Science & Technology, 56, 12873-12885, 10.1021/acs.est.2c02202, 2022.

Jones, A., Thomson, D., Hort, M., and Devenish, B.: The U.K. Met Office's Next-Generation Atmospheric Dispersion Model, NAME III, Air Pollution Modeling and Its Application XVII, Boston, MA, 2007//, 580-589,

Kroll, J. H. and Seinfeld, J. H.: Chemistry of secondary organic aerosol: Formation and evolution of low-volatility organics in the atmosphere, Atmospheric Environment, 42, 3593-3624, https://doi.org/10.1016/j.atmosenv.2008.01.003, 2008.

Kukui, A.: ACROSS_LPC2E_Rambforest_OH_L2 [dataset], https://doi.org/10.25326/510 2023.

Kukui, A., Ancellet, G., and Le Bras, G.: Chemical ionisation mass spectrometer for measurements of OH and Peroxy radical concentrations in moderately polluted atmospheres, Journal of Atmospheric Chemistry, 61, 133-154, 10.1007/s10874-009-9130-9, 2008.

Laskin, A., Laskin, J., and Nizkorodov, S. A.: Chemistry of Atmospheric Brown Carbon, Chemical Reviews, 115, 4335-4382, 10.1021/cr5006167, 2015.

Lee, A. K. Y., Abbatt, J. P. D., Leaitch, W. R., Li, S. M., Sjostedt, S. J., Wentzell, J. J. B., Liggio, J., and Macdonald, A. M.: Substantial secondary organic aerosol formation in a coniferous forest: observations of both day- and nighttime chemistry, Atmos. Chem. Phys., 16, 6721-6733, 10.5194/acp-16-6721-2016, 2016.

Li, Q., Liu, D., Jiang, X., Tian, P., Wu, Y., Li, S., Hu, K., Liu, Q., Huang, M., Li, R., Bi, K., Kong, S., Ding, D., and Yu, C.: Concurrent photochemical whitening and darkening of ambient brown carbon, Atmos. Chem. Phys., 23, 9439-9453, 10.5194/acp-23-9439-2023, 2023.

Lin, C., Ceburnis, D., Xu, W., Heffernan, E., Hellebust, S., Gallagher, J., Huang, R. J., O'Dowd, C., and Ovadnevaite, J.: The impact of traffic on air quality in Ireland: insights from the simultaneous kerbside and suburban monitoring of submicron aerosols, Atmos. Chem. Phys., 20, 10513-10529, 10.5194/acp-20-10513-2020, 2020.

Liu, D., Li, S., Hu, D., Kong, S., Cheng, Y., Wu, Y., Ding, S., Hu, K., Zheng, S., Yan, Q., Zheng, H., Zhao, D., Tian, P., Ye, J., Huang, M., and Ding, D.: Evolution of Aerosol Optical Properties from Wood Smoke in Real Atmosphere Influenced by Burning Phase and Solar Radiation, Environmental Science & Technology, 55, 5677-5688, 10.1021/acs.est.0c07569, 2021.

Lu, Z., Zhang, Q., and Streets, D. G.: Sulfur dioxide and primary carbonaceous aerosol emissions in China and India, 1996–2010, Atmos. Chem. Phys., 11, 9839-9864, 10.5194/acp-11-9839-2011, 2011.

Manisalidis, I., Stavropoulou, E., Stavropoulos, A., and Bezirtzoglou, E.: Environmental and Health Impacts of Air Pollution: A Review, Frontiers in Public Health, Volume 8 - 2020, 10.3389/fpubh.2020.00014, 2020.

Mei, F., Hayes, P. L., Ortega, A., Taylor, J. W., Allan, J. D., Gilman, J., Kuster, W., de Gouw, J., Jimenez, J. L., and Wang, J.: Droplet activation properties of organic aerosols observed at an urban site during CalNex-LA, Journal of Geophysical Research: Atmospheres, 118, 2903-2917, https://doi.org/10.1002/jgrd.50285, 2013.

Menut, L., Cholakian, A., Siour, G., Lapere, R., Pennel, R., Mailler, S., and Bessagnet, B.: Impact of Landes forest fires on air quality in France during the 2022 summer, Atmos. Chem. Phys., 23, 7281-7296, 10.5194/acp-23-7281-2023, 2023.

https://doi.org/10.5194/egusphere-2025-2667
Preprint. Discussion started: 7 July 2025

Michoud, V. and Bouzidi, H.: ACROSS_2022_RambForest_LISA_PTRMS_VOCs_Belowcanopy_10min_20220617 - 20220723, https://doi.org/10.25326/685 2024.

Mollner, A. K., Valluvadasan, S., Feng, L., Sprague, M. K., Okumura, M., Milligan, D. B., Bloss, W. J., Sander, S. P., Martien, P. T., Harley, R. A., McCoy, A. B., and Carter, W. P. L.: Rate of Gas Phase Association of Hydroxyl Radical and Nitrogen Dioxide, Science, 330, 646-649, 10.1126/science.1193030, 2010.

Nault, B. A., Campuzano-Jost, P., Day, D. A., Schroder, J. C., Anderson, B., Beyersdorf, A. J., Blake, D. R., Brune, W. H., Choi, Y., Corr, C. A., de Gouw, J. A., Dibb, J., DiGangi, J. P., Diskin, G. S., Fried, A., Huey, L. G., Kim, M. J., Knote, C. J., Lamb, K. D., Lee, T., Park, T., Pusede, S. E., Scheuer, E., Thornhill, K. L., Woo, J. H., and Jimenez, J. L.: Secondary organic aerosol production from local emissions dominates the organic aerosol budget over Seoul, South Korea, during KORUS-AQ, Atmos. Chem. Phys., 18, 17769-17800, 10.5194/acp-18-17769-2018, 2018.

Ng, N. L., Herndon, S. C., Trimborn, A., Canagaratna, M. R., Croteau, P. L., Onasch, T. B., Sueper, D., Worsnop, D. R., Zhang, Q., Sun, Y. L., and Jayne, J. T.: An Aerosol Chemical Speciation Monitor (ACSM) for Routine Monitoring of the Composition and Mass Concentrations of Ambient Aerosol, Aerosol Science and Technology, 45, 780-794, 10.1080/02786826.2011.560211, 2011.

Nguyen, T. B., Crounse, J. D., Teng, A. P., St. Clair, J. M., Paulot, F., Wolfe, G. M., and Wennberg, P. O.: Rapid deposition of oxidized biogenic compounds to a temperate forest, Proceedings of the National Academy of Sciences, 112, E392-E401, doi:10.1073/pnas.1418702112, 2015.

Petit, J. E., Favez, O., Sciare, J., Crenn, V., Sarda-Estève, R., Bonnaire, N., Močnik, G., Dupont, J. C., Haeffelin, M., and Leoz-Garziandia, E.: Two years of near real-time chemical composition of submicron aerosols in the region of Paris using an Aerosol Chemical Speciation Monitor (ACSM) and a multi-wavelength Aethalometer, Atmos. Chem. Phys., 15, 2985-3005, 10.5194/acp-15-2985-2015, 2015.

Petzold, A., Ogren, J. A., Fiebig, M., Laj, P., Li, S. M., Baltensperger, U., Holzer-Popp, T., Kinne, S., Pappalardo, G., Sugimoto, N., Wehrli, C., Wiedensohler, A., and Zhang, X. Y.: Recommendations for reporting "black carbon" measurements, Atmos. Chem. Phys., 13, 8365-8379, 10.5194/acp-13-8365-2013, 2013.

Ravishankara, A. R., Rudich, Y., and Wuebbles, D. J.: Physical Chemistry of Climate Metrics, Chemical Reviews, 115, 3682-3703, 10.1021/acs.chemrev.5b00010, 2015.

Riva, M., Budisulistiorini, S. H., Chen, Y., Zhang, Z., D'Ambro, E. L., Zhang, X., Gold, A., Turpin, B. J., Thornton, J. A., Canagaratna, M. R., and Surratt, J. D.: Chemical Characterization of Secondary Organic Aerosol from Oxidation of Isoprene Hydroxyhydroperoxides, Environmental Science & Technology, 50, 9889-9899, 10.1021/acs.est.6b02511, 2016.

Romer, P. S., Duffey, K. C., Wooldridge, P. J., Allen, H. M., Ayres, B. R., Brown, S. S., Brune, W. H., Crounse, J. D., de Gouw, J., Draper, D. C., Feiner, P. A., Fry, J. L., Goldstein, A. H., Koss, A., Misztal, P. K., Nguyen, T. B., Olson, K., Teng, A. P., Wennberg, P. O., Wild, R. J., Zhang, L., and Cohen, R. C.: The lifetime of nitrogen oxides in an isoprene-dominated forest, Atmos. Chem. Phys., 16, 7623-7637, 10.5194/acp-16-7623-2016, 2016.

Schmale, J., Schneider, J., Nemitz, E., Tang, Y. S., Dragosits, U., Blackall, T. D., Trathan, P. N., Phillips, G. J., Sutton, M., and Braban, C. F.: Sub-Antarctic marine aerosol: dominant contributions from biogenic sources, Atmos. Chem. Phys., 13, 8669-8694, 10.5194/acp-13-8669-2013, 2013.

Seinfeld, J. H. and Pandis, S. N.: Atmospheric Chemistry and Physics: From Air Pollution to Climate Change, Wiley2016.

Shi, Z., Vu, T., Kotthaus, S., Harrison, R. M., Grimmond, S., Yue, S., Zhu, T., Lee, J., Han, Y., Demuzere, M., Dunmore, R. E., Ren, L., Liu, D., Wang, Y., Wild, O., Allan, J., Acton, W. J., Barlow, J., Barratt, B., Beddows, D., Bloss, W. J., Calzolai, G., Carruthers, D., Carslaw, D. C., Chan, Q., Chatzidiakou, L., Chen, Y., Crilley, L., Coe, H., Dai, T., Doherty, R., Duan, F., Fu, P., Ge, B., Ge, M., Guan, D., Hamilton, J. F., He, K., Heal, M., Heard, D., Hewitt, C. N., Hollaway, M., Hu, M., Ji, D., Jiang, X., Jones, R., Kalberer, M., Kelly, F. J., Kramer, L., Langford, B., Lin, C., Lewis, A. C., Li, J., Li, W., Liu, H., Liu, J., Loh, M., Lu, K., Lucarelli, F., Mann, G., McFiggans, G., Miller, M. R., Mills, G., Monk, P., Nemitz, E., O'Connor, F., Ouyang, B., Palmer, P. I., Percival, C., Popoola, O., Reeves, C., Rickard, A. R., Shao, L., Shi, G., Spracklen, D., Stevenson, D., Sun, Y., Sun, Z., Tao, S., Tong, S., Wang, Q., Wang, W., Wang, X., Wang, X., Wang, Z., Wei, L., Whalley, L., Wu, X., Wu, Z., Xie, P., Yang, F., Zhang, Q., Zhang, Y., Zhang, Y., and Zheng, M.: Introduction to the

https://doi.org/10.5194/egusphere-2025-2667
Preprint. Discussion started: 7 July 2025

special issue “In-depth study of air pollution sources and processes within Beijing and its surrounding region (APHH-Beijing)”, Atmos. Chem. Phys., 19, 7519-7546, 10.5194/acp-19-7519-2019, 2019.

Stirnberg, R., Cermak, J., Kotthaus, S., Haeffelin, M., Andersen, H., Fuchs, J., Kim, M., Petit, J. E., and Favez, O.: Meteorology-driven variability of air pollution (PM1) revealed with explainable machine learning, Atmos. Chem. Phys., 21, 3919-3948, 10.5194/acp-21-3919-2021, 2021.

Tuet, W. Y., Chen, Y., Xu, L., Fok, S., Gao, D., Weber, R. J., and Ng, N. L.: Chemical oxidative potential of secondary organic aerosol (SOA) generated from the photooxidation of biogenic and anthropogenic volatile organic compounds, Atmos. Chem. Phys., 17, 839-853, 10.5194/acp-17-839-2017, 2017.

Tuet, W. Y., Fok, S., Verma, V., Tagle Rodriguez, M. S., Grosberg, A., Champion, J. A., and Ng, N. L.: Dose-dependent intracellular reactive oxygen and nitrogen species (ROS/RNS) production from particulate matter exposure: comparison to oxidative potential and chemical composition, Atmospheric Environment, 144, 335-344, https://doi.org/10.1016/j.atmosenv.2016.09.005, 2016.

Ulbrich, I. M., Canagaratna, M. R., Zhang, Q., Worsnop, D. R., and Jimenez, J. L.: Interpretation of organic components from Positive Matrix Factorization of aerosol mass spectrometric data, Atmos. Chem. Phys., 9, 2891-2918, 10.5194/acp-9-2891-2009, 2009.

Wang, Y., Voliotis, A., Hu, D., Shao, Y., Du, M., Chen, Y., Kleinheins, J., Marcolli, C., Alfarra, M. R., and McFiggans, G.: On the evolution of sub- and super-saturated water uptake of secondary organic aerosol in chamber experiments from mixed precursors, Atmos. Chem. Phys., 22, 4149-4166, 10.5194/acp-22-4149-2022, 2022.

Wang, Y., Li, Z., Zhang, Y., Du, W., Zhang, F., Tan, H., Xu, H., Fan, T., Jin, X., Fan, X., Dong, Z., Wang, Q., and Sun, Y.: Characterization of aerosol hygroscopicity, mixing state, and CCN activity at a suburban site in the central North China Plain, Atmos. Chem. Phys., 18, 11739-11752, 10.5194/acp-18-11739-2018, 2018.

Wu, Y., Liu, D., Tian, P., Sheng, J., Liu, Q., Li, R., Hu, K., Jiang, X., Li, S., Bi, K., Zhao, D., Huang, M., Ding, D., and Wang, J.: Tracing the Formation of Secondary Aerosols Influenced by Solar Radiation and Relative Humidity in Suburban Environment, Journal of Geophysical Research: Atmospheres, 127, e2022JD036913, https://doi.org/10.1029/2022JD036913, 2022.

Wu, Y., Liu, Q., Liu, D., Tian, P., Xu, W., Wang, J., Hu, K., Li, S., Jiang, X., Wang, F., Huang, M., Ding, D., Yu, C., and Hu, D.: Enhanced formation of nitrogenous organic aerosols and brown carbon after aging in the planetary boundary layer, npj Climate and Atmospheric Science, 7, 179, 10.1038/s41612-024-00726-x, 2024.

Yang, J., Au, W. C., Law, H., Lam, C. H., and Nah, T.: Formation and evolution of brown carbon during aqueous-phase nitrate-mediated photooxidation of guaiacol and 5-nitroguaiacol, Atmospheric Environment, 254, 118401, https://doi.org/10.1016/j.atmosenv.2021.118401, 2021.

Yu, C., Pasternak, D., Lee, J., Yang, M., Bell, T., Bower, K., Wu, H., Liu, D., Reed, C., Bauguitte, S., Cliff, S., Trembath, J., Coe, H., and Allan, J. D.: Characterizing the Particle Composition and Cloud Condensation Nuclei from Shipping Emission in Western Europe, Environmental Science & Technology, 54, 15604-15612, 10.1021/acs.est.0c04039, 2020.

Yus-Díez, J., Bernardoni, V., Močnik, G., Alastuey, A., Ciniglia, D., Ivančič, M., Querol, X., Perez, N., Reche, C., Rigler, M., Vecchi, R., Valentini, S., and Pandolfi, M.: Determination of the multiple-scattering correction factor and its cross-sensitivity to scattering and wavelength dependence for different AE33 Aethalometer filter tapes: a multi-instrumental approach, Atmos. Meas. Tech., 14, 6335-6355, 10.5194/amt-14-6335-2021, 2021.

Zaveri, R. A., Wang, J., Fan, J., Zhang, Y., Shilling, J. E., Zelenyuk, A., Mei, F., Newsom, R., Pekour, M., Tomlinson, J., Comstock, J. M., Shrivastava, M., Fortner, E., Machado, L. A. T., Artaxo, P., and Martin, S. T.: Rapid growth of anthropogenic organic nanoparticles greatly alters cloud life cycle in the Amazon rainforest, Science Advances, 8, eabj0329, doi:10.1126/sciadv.abj0329, 2022.

Zhang, Y., Favez, O., Petit, J. E., Canonaco, F., Truong, F., Bonnaire, N., Crenn, V., Amodeo, T., Prévôt, A. S. H., Sciare, J., Gros, V., and Albinet, A.: Six-year source apportionment of submicron organic aerosols from near-continuous highly time-resolved measurements at SIRTA (Paris area, France), Atmos. Chem. Phys., 19, 14755-14776, 10.5194/acp-19-14755-2019, 2019.

Zhao, R., Lee, A. K. Y., Huang, L., Li, X., Yang, F., and Abbatt, J. P. D.: Photochemical processing of aqueous atmospheric brown carbon, Atmos. Chem. Phys., 15, 6087-6100, 10.5194/acp-15-6087-2015, 2015.

https://doi.org/10.5194/egusphere-2025-2667
Preprint. Discussion started: 7 July 2025

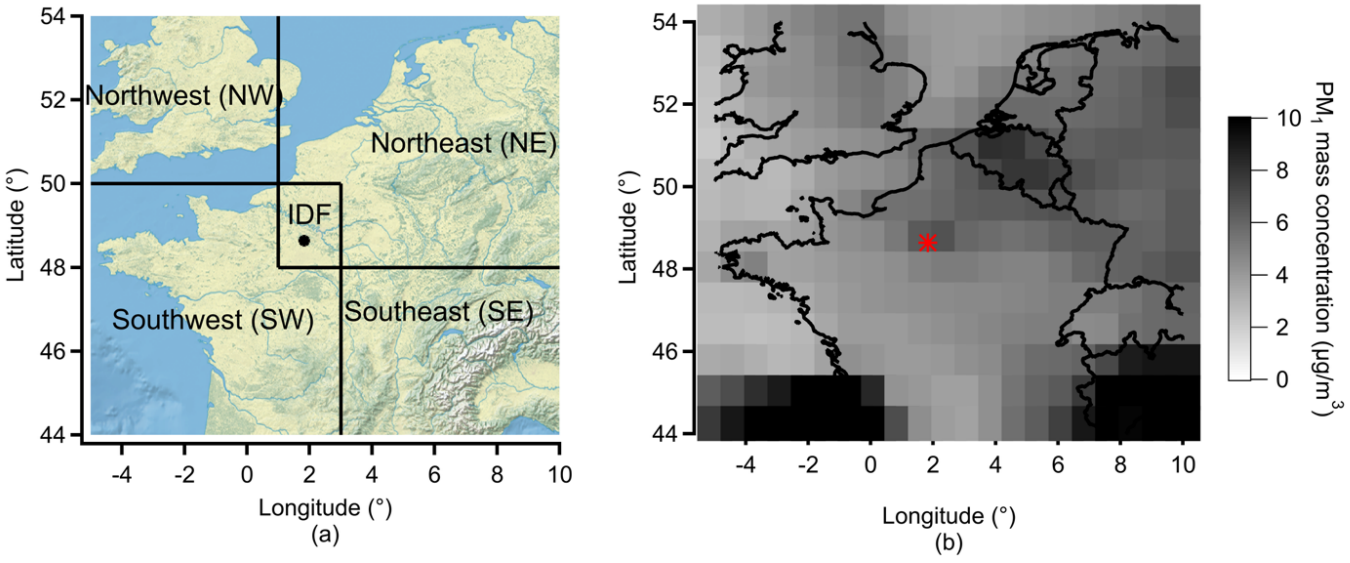

760 **Figure 1: (a) Classification of the potential air mass source regions; (b) ECMWF CAMS EAC4 (ECMWF Atmospheric Composition Reanalysis 4) reanalysis PM_1 spatial distribution during the ACROSS campaign period. The dot in the figure represents the location of the Rambouillet measurement site. (the map information is from © Google Maps).**

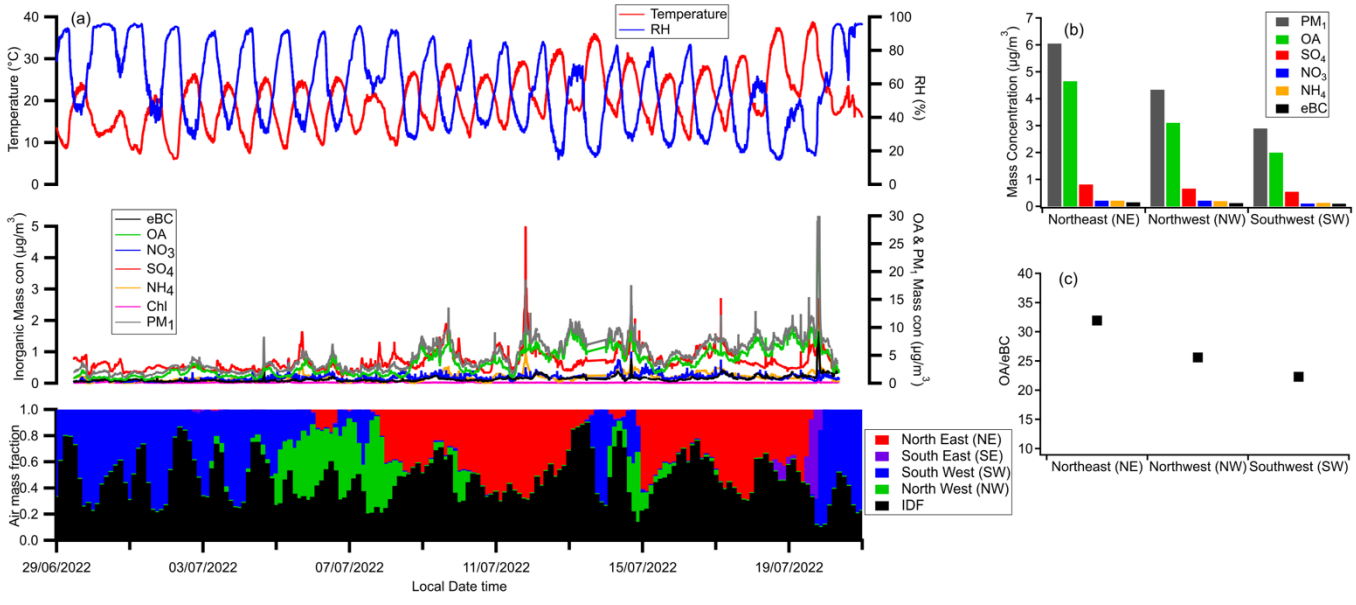

765 **Figure 2: (a) Time series of temperature, RH, PM_1 and historic air mass fractions; (b) The average PM_1 composition mass concentrations under different external air mass dominated periods; (c) The average normalised OA under different external air mass dominated periods.**

https://doi.org/10.5194/egusphere-2025-2667
Preprint. Discussion started: 7 July 2025

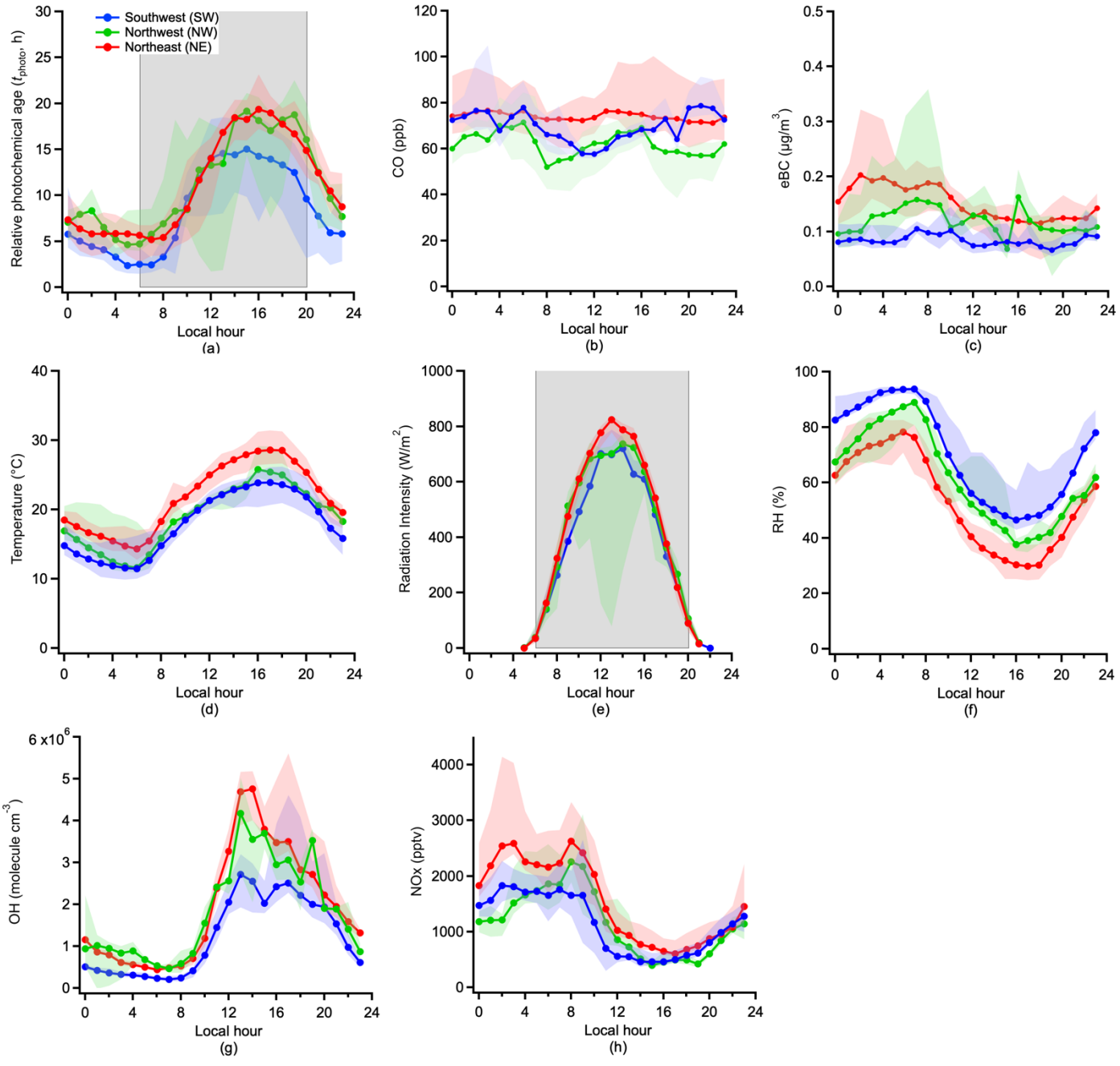

Figure 3: Diurnal variation of the (a) Relative photochemical age; (b) CO mixing ratio; (c) eBC mass concentration; (d) Temperature; (e) Radiation Intensity; (f) RH; (g) OH concentration; (h) NO_x concentration. The grey shades in (a) and (e) indicate the periods for the photochemical aging analysis. The lower and upper whiskers in the figure are the 25th and 75th percentiles, respectively.

https://doi.org/10.5194/egusphere-2025-2667
Preprint. Discussion started: 7 July 2025

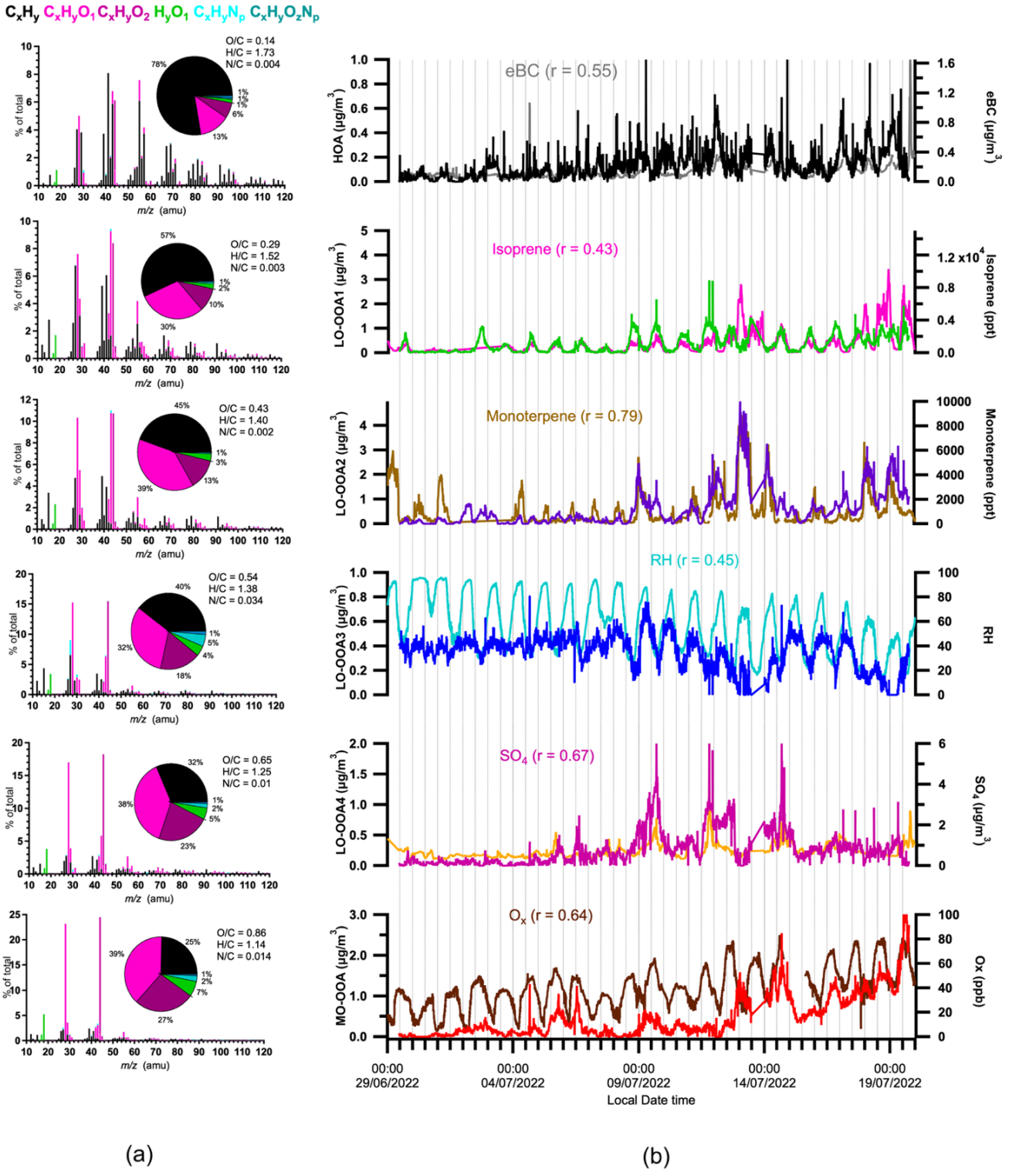

775 **Figure 4: Results of the positive matrix factor (PMF) analysis of OA: (a) Average mass spectra; and (b) Time series.**

https://doi.org/10.5194/egusphere-2025-2667
Preprint. Discussion started: 7 July 2025

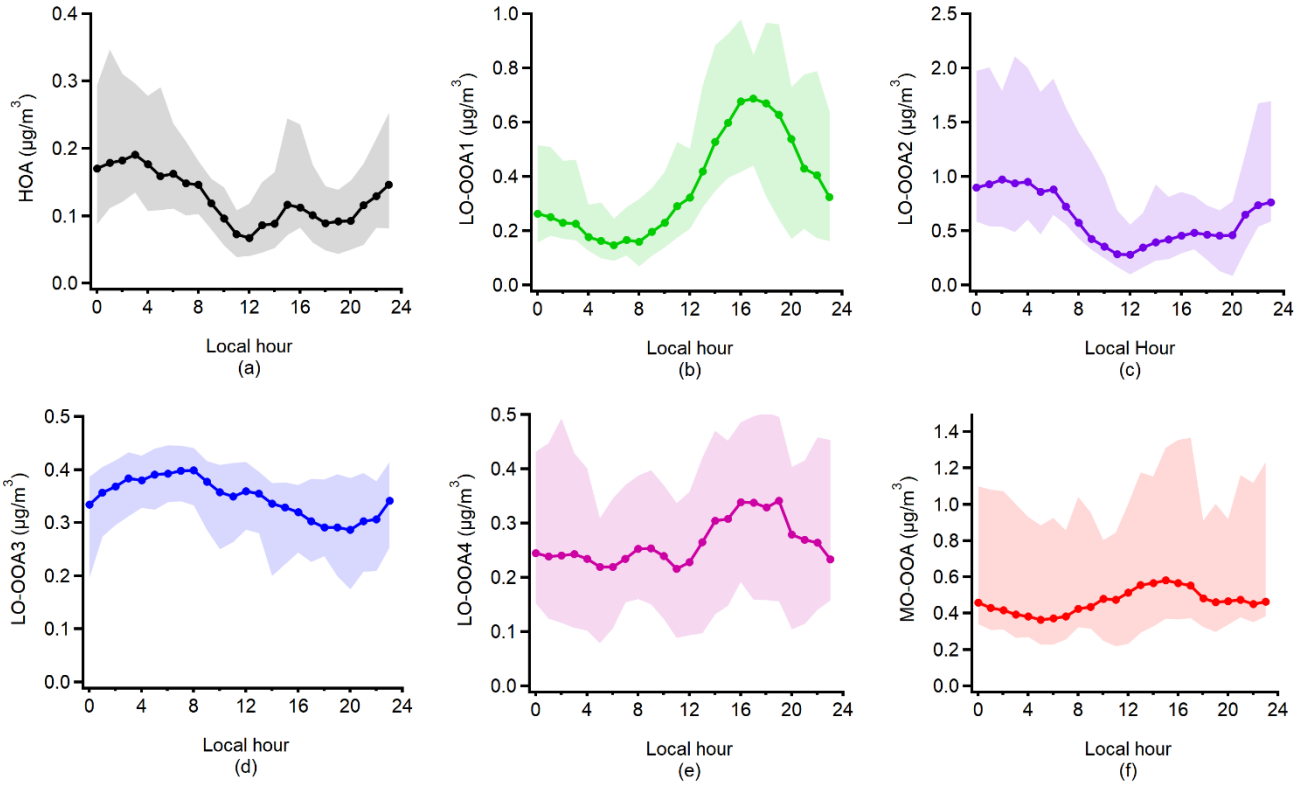

Figure 5: Diurnal variation of all the PMF OA factors. The lower and upper whiskers in the figure are the 25th and 75th percentiles, respectively.

780

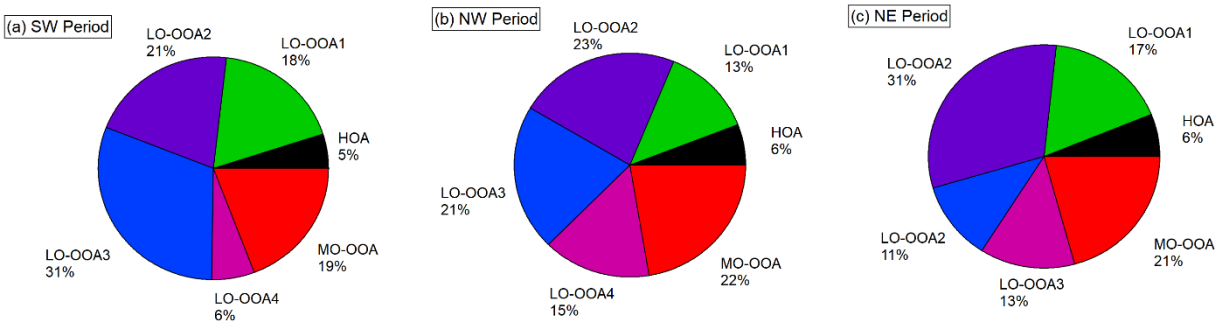

Figure 6: Pie charts for the mass fractions of different PMF OA factors during the three different airmass dominated periods

https://doi.org/10.5194/egusphere-2025-2667
Preprint. Discussion started: 7 July 2025

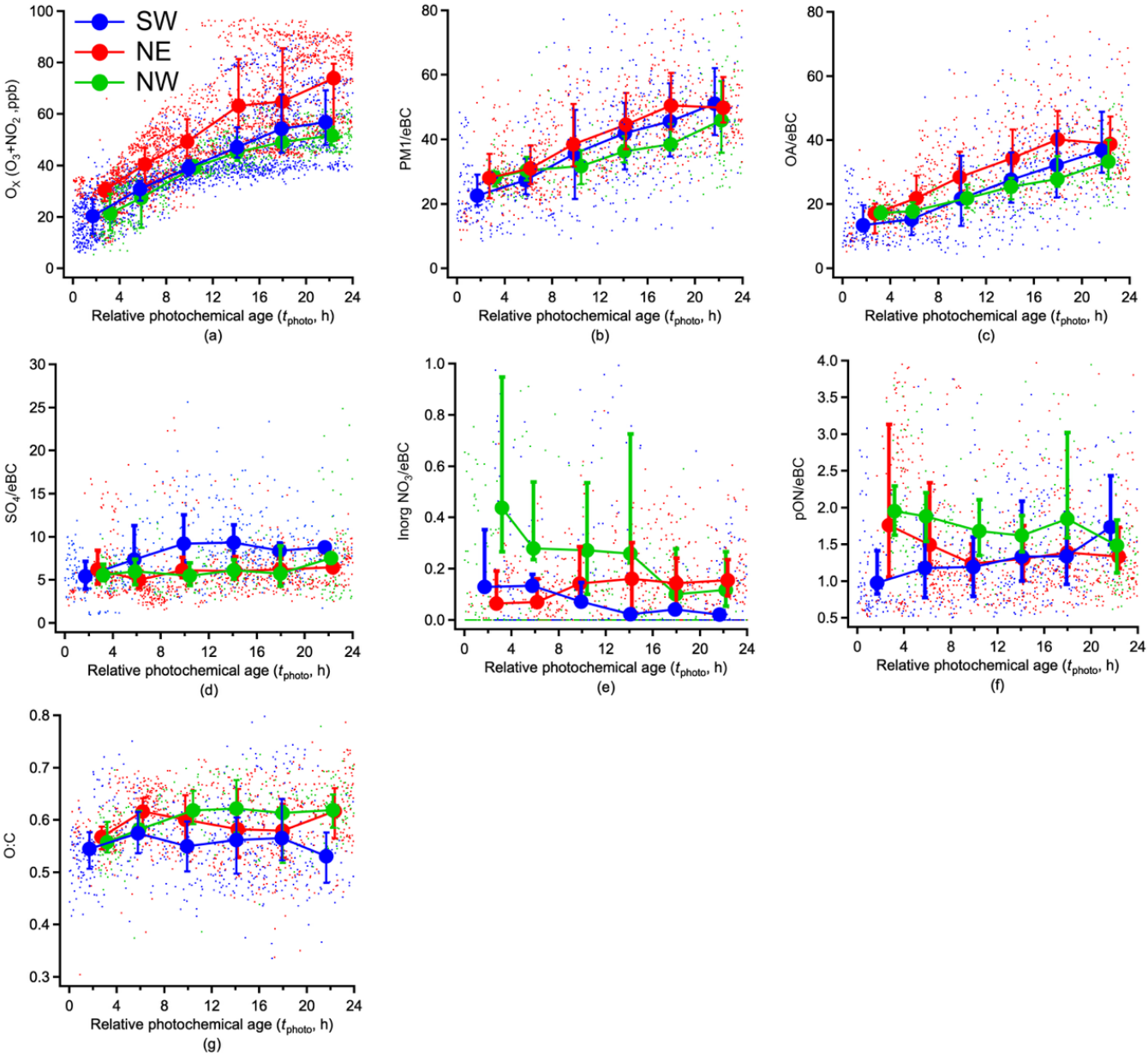

Figure 7: Variations in aerosol compositions concentrations: (a) O_x (O_3+NO_2) (b) PM_1 (c)OA (d) Sulfate (e) Inorganic nitrate (f) particulate Organic Nitrate (pON) (g) O:C ratio measured by HR-AMS as a function of relative photochemical age. The results are averaged into four-hour intervals along t_{photo} and the error bar indicates the 25th and 75th percentiles, respectively.

https://doi.org/10.5194/egusphere-2025-2667
Preprint. Discussion started: 7 July 2025

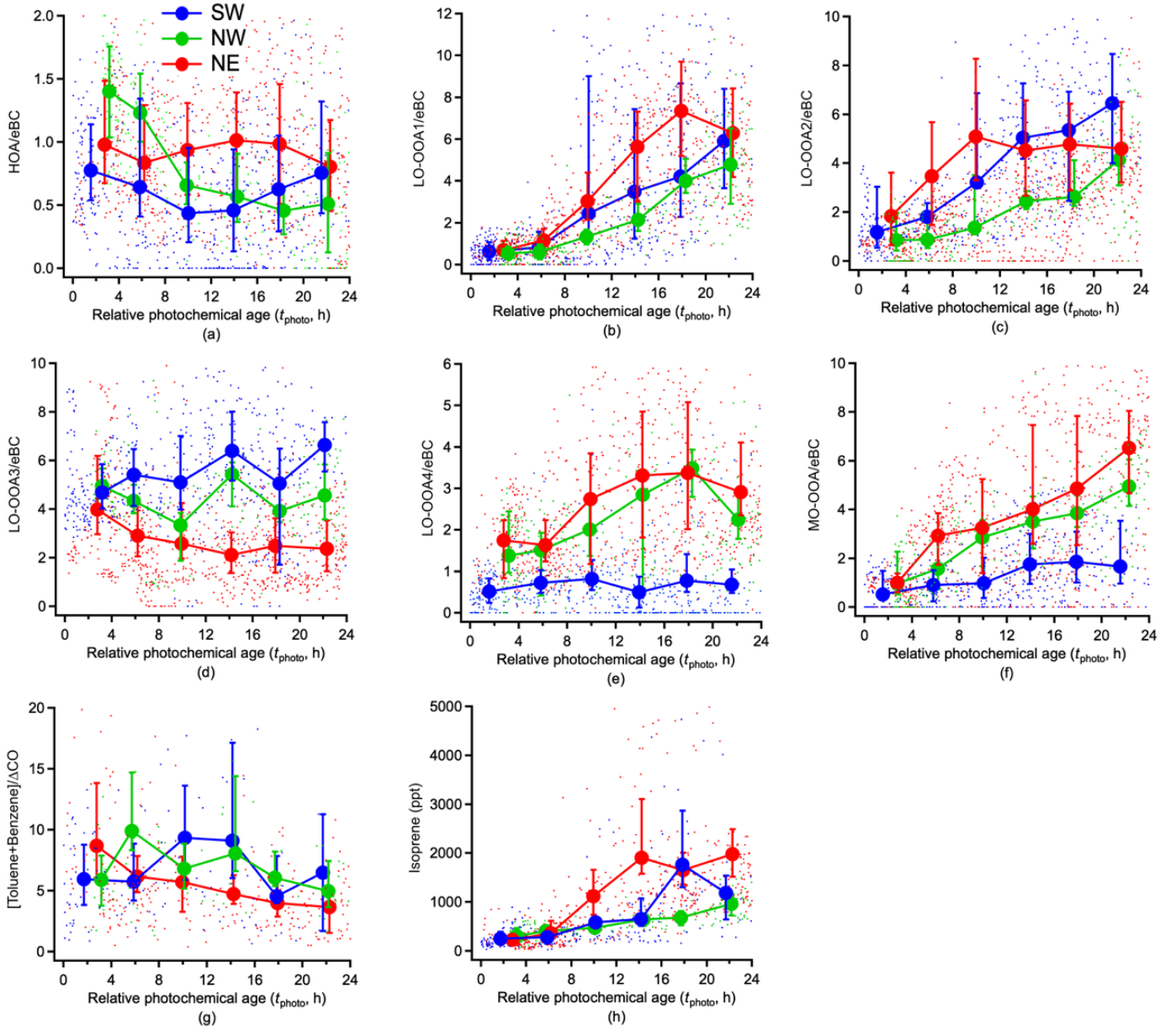

Figure 8: Variations in (a-f) HR-AMS PMF-derived factors normalised concentrations; (g) Sum of Toluene and Benzene normalised concentration; (h) isoprene concentration as a function of relative photochemical age. The results are averaged into four-hour intervals along t_{photo} and the error bar indicates the 25th and 75th percentiles, respectively.

https://doi.org/10.5194/egusphere-2025-2667
Preprint. Discussion started: 7 July 2025

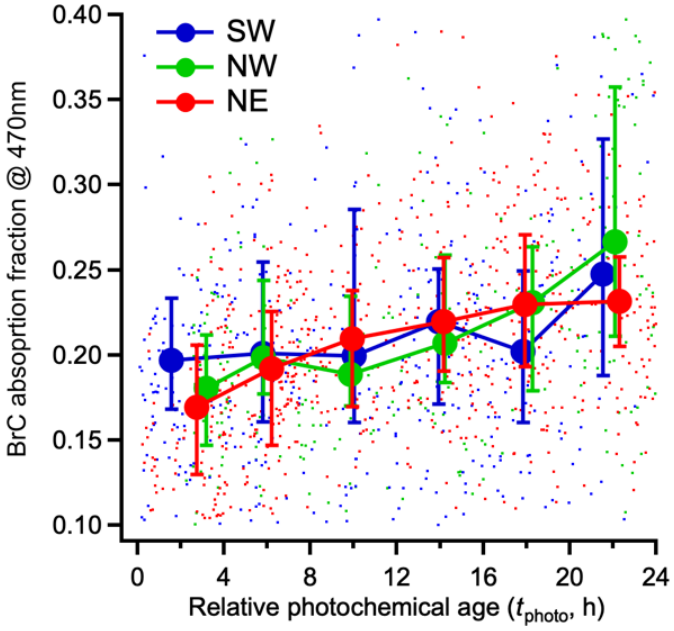

Figure 9 Variations of absorption fraction of BrC at 470 nm as a function of relative photochemical age. The results are averaged into four-hour intervals along t_{photo} and the error bar indicates the 25th and 75th percentiles, respectively.

$\sigma_{abs\ BrC,470}$ (R^2 = 0.54)		
HR-AMS PMF factor	Regression coefficient a_i	Partial correlation coefficient
HOA	0.47	0.53
LO-OOA1	-	-
LO-OOA2	0.04	0.58
LO-OOA3	0.57	-0.25
LO-OOA4	0.30	0.55
MO-OOA	0.40	0.86
Intercept		-0.13

795 **Table 1 Results of multiple linear regression (MLR) between $\sigma_{abs\ BrC,470}$ and individual PMF-derived factors. The final regression excludes the LO-OOA1 due to its negative regression coefficient value (-0.06). Results include all the PMF-derived factors are presented in Table S2 in the supplementary.**